Iron Complexes with Tetradentate Aromatic Ligands for Photocatalytic Hydrogen Generation

Jessica Danielle Cropley

Hampton, Virginia

Associate of Science, Thomas Nelson Community College, 2019

Bachelor of Science, Christopher Newport University, 2021

A Thesis presented to the Graduate Faculty of The College of William & Mary in Candidacy for the Degree of
Master of Science

Department of Chemistry

College of William & Mary
May 2023

APPROVAL PAGE

This Thesis is submitted in partial fulfillment of
the requirements for the degree of

Master of Science

Jessica Cropley

Jessica Danielle Cropley

Approved by the Committee, April 2023

WR

Committee Chair
William R. McNamara, Associate Professor, Chemistry
College of William & Mary

J.C. Poutsma, Professor, Chemistry
College of William & Mary

Nathan Kidwell

Nathan M. Kidwell, Associate Professor, Chemistry
College of William & Mary

ABSTRACT

Fossil fuels are a critical component of the world's current energy system and have sustained a 10-fold global population growth since the Industrial Revolution. However, the combustion of fossil fuels has negatively impacted the health of the environment and atmosphere. Artificial photosynthesis (AP) is a promising energy alternative to fossil fuels that can generate hydrogen gas as a fuel source from aqueous solutions with a catalyst, chromophore, and electron donor system. Hydrogen is a highly desirable fuel source, as the only products from hydrogen fuel cells are electricity and pure water. It is vital to discover novel catalysts for hydrogen generation. Precious metal catalysts are cost prohibitive and rare, which can restrict scaling hydrogen production up to industrial levels. Optimizing catalysts using earth-abundant first row transition metals to be covalently bonded to TiO_2 nanoparticles (NP) can be a stable, efficient, and cost-effective alternative to precious metal catalytic systems. By immobilizing effective molecular catalysts on TiO_2, the catalyst can be recycled after the degradation of the chromophore and electron donor for additional hydrogen generation, and can be utilized in sea water to produce fuel and pure water from impure water systems.

TABLE OF CONTENTS

ACKNOWLEDGEMENTS

I would like to thank Professor McNamara for his invaluable help with the research and writing of this thesis and always keeping me on my toes. You have been a great guide throughout my time in graduate school, and I am very grateful the way you tailored my experience to help bolster my strengths and help me grow as both a chemist and a person.

I am eternally grateful to everyone in our lab, you have all made this a joyous experience, always full of laughter, music, camaraderie, and interesting chemical smells. I'd like to extend a special thank you to Marissa for much needed pep talks and walky-walks and to Tim for helping me remember that we can do big things.

I could not have completed this without the support of my wonderful family. Thanks to my husband, Shawn, whose constant encouragement helped me through the tough times, and for always being willing to celebrate the little wins throughout this process. A big thank you to my mom, Kathy, who always listened to my struggles, both big and small, and always offered a helpful word or a shoulder to cry on.

I would also like to thank my committee members Professor Kidwell and Professor Poutsma for the wonderful guidance and helpful conversations through my time at W&M.

I am forever thankful to the entire community at W&M for being so welcoming and supportive, especially the chemistry department. And to my fellow graduate students, especially Laurel, I'm eternally grateful that we went through this together.

You have all made this a highlight in my life, and I will always cherish my times here.

LIST OF TABLES

LIST OF FIGURES

Chapter 1. Introduction

The Global Impact of Fossil Fuels

Since the industrial revolution, humans have been burning coal and fossil fuels to generate energy to sustain an ever-growing population. A population boom has occurred in the years since, growing from 770 million in 1760, around the advent of the steam engine, to over 7.9 billion in the year 2021.[1] This 10-fold population increase has generated the need for more and more power, with 18.9 TW of power used globally in 2021, and nearly 80% of this energy being generated from fossil fuels (Figure 1.1).[2] While energy consumption dipped in 2020 due to the coronavirus pandemic hampering industry and travel, global consumption has rebounded and nearly returned pre-pandemic levels, and are expected to nearly double by 2050.[3]

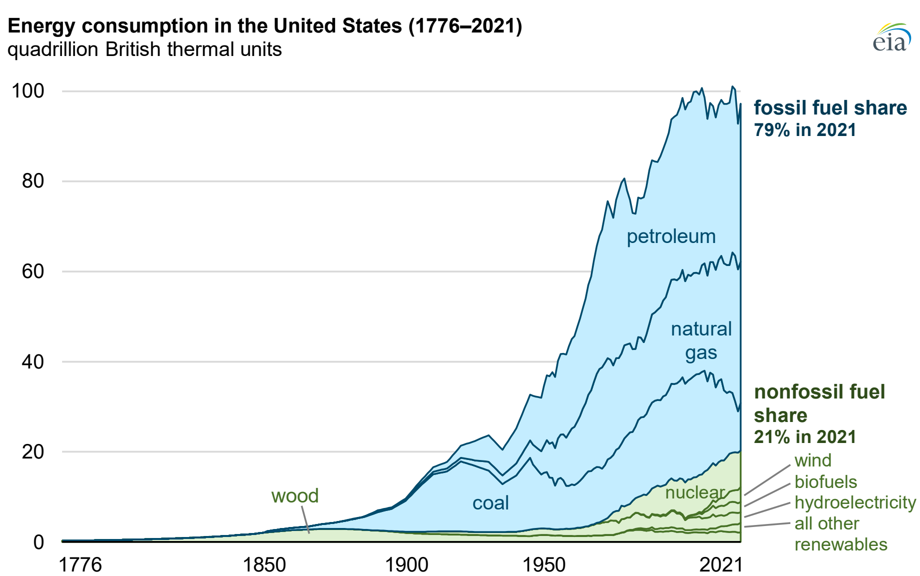

Figure 1.1. Energy consumption in the United States from 1776-2021.[2]

Fossil fuel reserve estimations state that an energy consumption of 30 TW per year can be sustained for several centuries,[4] but the use of fossil fuels for energy comes at the detriment of the health of the population and atmosphere. A 2019 study found that 18% of global deaths were directly caused by pollutants from fossil fuel combustion and a 2016 study by the World Health Organization determined over 169,000 deaths of children under five were caused by fossil fuel pollution.[5]

This illustrates the dangers of being in the immediate area of combustion of fossil fuels, but negative effects are felt throughout the globe as the concentrations of greenhouse gasses, such as methane and carbon dioxide, continue to increase in our atmosphere. There is a direct correlation between the use of fossil fuels and atmospheric carbon dioxide (CO_2) levels (Figure 1.2), with pre industrial CO_2 levels near 280 ppm while current CO_2 levels are exceeding 400 ppm.[6] Advanced atmospheric CO_2 monitoring has been in effect since the late 1950s, and scientists have been able to use air bubbles in ice samples from Greenland and Antarctica to determine the CO_2 levels of around 280 ppm were steady for over 10,000 years before the Industrial Revolution beginning in the 1750s.[7] Within the last decade, CO_2 concentrations have been rising at an average of 2.4 ppm annually, a 100-fold increase over the greatest natural increase in CO_2 levels before the end of the last ice age.[6]

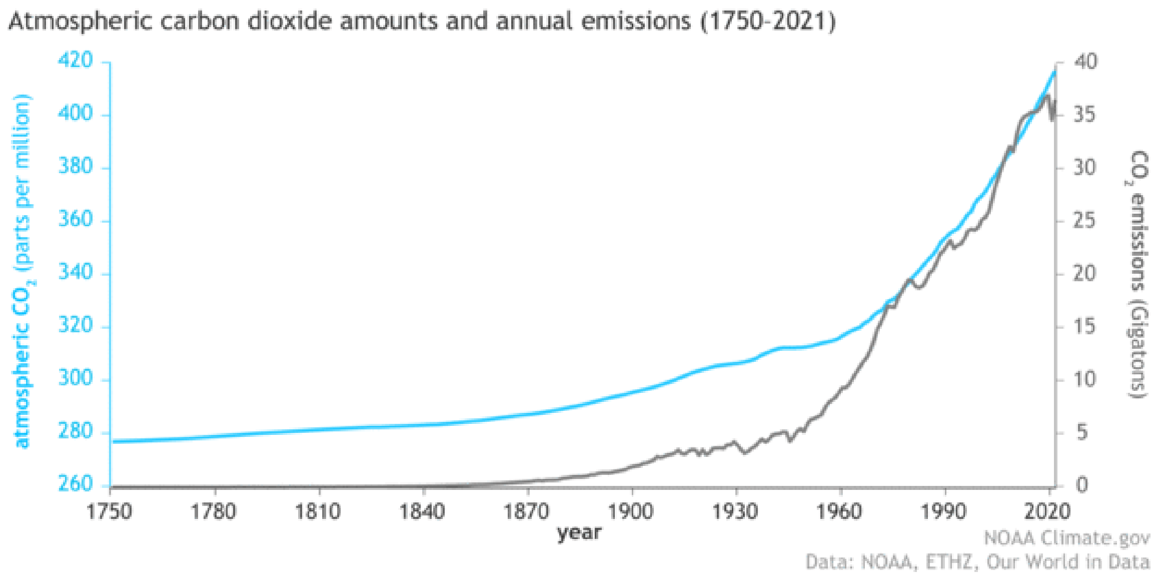

Figure 1.2. Atmospheric CO_2 levels in ppm (blue) and CO_2 emissions in gigatons (black) from 1750 to 2020.[6]

Increased CO_2 levels have led to a change in the pH of the oceans, with a 26% increase in acidity corresponding to a 0.1 decrease in pH in the last 250 years, a 100-times faster increase than had ever been previously recorded. [8] This increasing acidity affects the levels of calcium carbonate in the sea water, which has an impact on shell formation of marine organisms, as well as coral growth due to decreased rates of calcification in more acidic environments. Changes like these are detrimental to all ocean life, as 25% of fish directly depend on coral reefs, and the reefs provide shelter and nourishment for a wide diversity of marine life.[9] Since coral reefs act also as a coastal barrier to waves and strong storms, a decrease in reefs may result in decreased protection against flooding, damage, and erosion to the coasts.[10]

Increased greenhouse gasses have a strong impact on the overall climate of Earth. Paleoclimatic research has been an interesting topic for researchers, and there is currently a climate record dating back over one million years that delineates the climate fluctuations and cycles that naturally occur. Based on this information, the Intergovernmental Panel on Climate Change (IPCC) concluded in 1990 that human emissions have substantially increased CO_2, methane (CH_4), chlorofluorocarbons (CFCs), and nitrogen dioxide (NO_2) in the atmosphere, with some of these gasses being known contributors to increased greenhouse warming.[7] Since then, the IPCC has reported that human-induced climate change has contributed to increased intensity and frequency of extreme weather events, heat-related mortality, areas affected by wildfires, droughts, damages occurring from tropical cyclones, and sea level rise. These changes have negatively impacted food and water security, leading to increased rates of malnutrition, with the greatest impacts on Indigenous populations, low income households, the elderly, pregnant women, and children.[11] In addition, climate change has contributed to decreased water security, causing roughly half the world's population to experience some time of severe water scarcity within the past year.[11]

Renewable resources

It is imperative to look for new sustainable and cleaner energy sources that don't have the same negative environmental impacts as fossil fuels. Renewable energy sources generated in the US, such as wind and solar, have increased nearly two-fold since 2018, and are projected to continue increasing (Figure 1.3).[12]

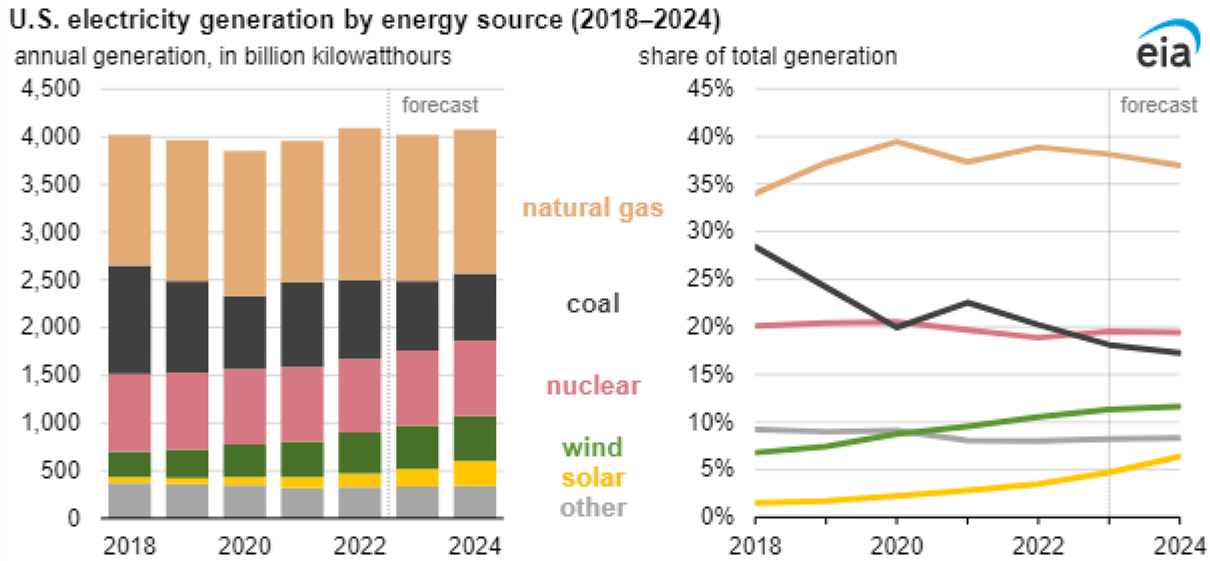

Figure 1.3. Distribution of energy generation in U.S. from 2018-2024.[12]

Wind energy is harvested by the kinetic energy of wind turning a turbine to generate rotational energy, which is then transformed into electricity using a generator. Since 2000, global wind turbine capacity has increased nearly 100-fold to allow for 733 GW of energy to be generated annually.[13] Turbines have become increasingly more efficient and are steadily decreasing in cost per unit of energy produced, but new wind turbine projects are not projected to maintain the same booming growth long term. This may be due to areas ideal for wind farming being in remote locations that do not have a connection to main energy grids, the noise and visual impact of the turbines, and the impact of the turbines on wildlife.[14]

Solar power is forecasted to continue increasing, with the main source of solar energy coming from photovoltaic cells, and a small fraction coming from solar thermal energy and artificial photosynthesis (AP). Solar thermal energy works by converting light to heat, as large areas of water or heat-conducting material are heated by sunlight. While the thermal energy can be stored in the material, allowing for use of the solar thermal energy at night, the efficacy of energy conversion is limited by surface area of the material. Overall, this process works well for heating air and water, but has limited electricity use.[15]

Photovoltaic (PV) cells are generally composed of semiconductor materials that, when photons are absorbed, transfer electrons throughout the material to generate a potential voltage from the imbalance of charge.[16] The conduction properties of a material can be explained by the arrangement of the valence band and conduction band. The valence band (VB) is where ground-state electrons reside and the conduction band (CB) is where electrons reside after excitation and allows for conduction and movement of electrons. The space between the valence and conduction band is known as the band gap (Figure 1.4). Metals have overlapping valence and conduction bands, and can therefore conduct electrons in any conditions, and insulators have too large of a band gap to excite electrons into the conduction bands, and so do not conduct electrons under most conditions. Between the two materials reside semiconductors, where the band gap is not overlapping but is small enough to be traversed by electrons excited by photons or thermal energy.

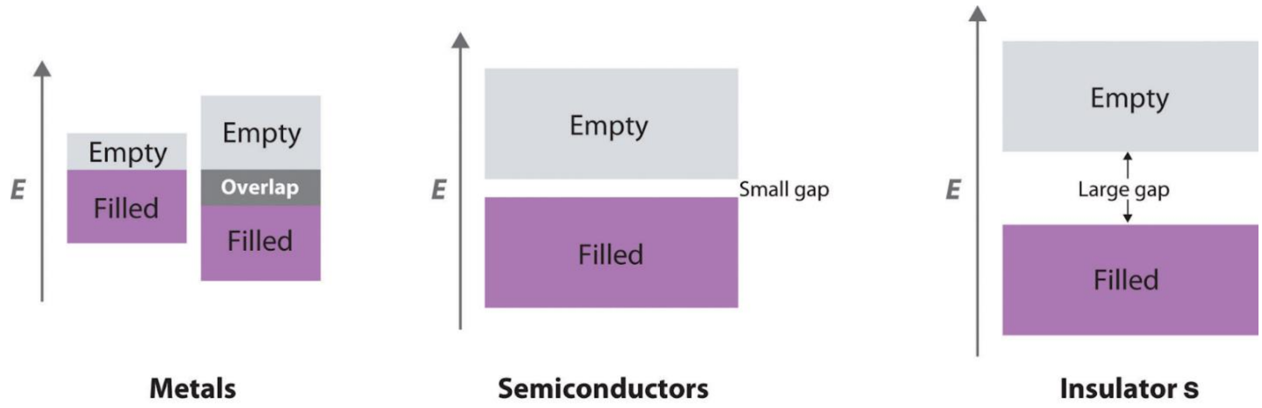

Figure 1.4. Diagram of band gaps for metals, semiconductors, and insulators.[17]

Semiconductor materials for commercial PV cells are over 90% crystalline silicon due to the abundance of silicon in the earth's crust, however there are many semiconductor possibilities that are being researched to grow PV technology. Some of the other semiconductors used include gallium arsenide, thin films composed of copper indium gallium diselenide (CIGS), cadmium telluride, perovskite, organic materials, or quantum dots.[18] These materials produce PV cells that have energy conversion efficiency of nearly 30%, with higher efficiencies for materials with multiple junctions. These junctions are interfaces of different semiconductor types that have differing properties and band gaps, allowing greater use of the energy from sunlight.[19]

Developers have planned to double the US's solar harvesting capacity to nearly 30 GW in 2024. Energy storage is becoming a limiting factor, as the US's current battery storage capacity is only 7.8 GW as of October 2022, though it is projected to grow rapidly in the coming years.[20] It is shown that PV cells have become increasingly efficient in generating electricity using sunlight, but battery capacity is a limitation for widespread use. Utilizing the sun's energy is a very sustainable way to generate electricity, but more storage options must be explored.

Artificial Photosynthesis

Artificial photosynthesis (AP) is a promising alternative to gathering solar energy because the energy is stored in chemical bonds rather than batteries. To design great AP catalysts, scientists must seek to understand natural photosynthesis. Plants and algae are observed to be a highly effective harvester of sunlight to produce energy from CO_2 and water using chlorophyll. Chlorophyll acts as a chromophore, which absorbs light and promotes an electron to an excited state. The electron is then transferred through the chromophore's sp^2 hybridized porphyrin structure, known as resonant energy transfer, to the reaction site and creates a charge separation.[21] The electron-hole pair is spatially separated, which allows for the oxidation of water to O_2 using the holes, and the reduction of CO_2 to sugar with the electron and proton. This is a highly effective process that has been refined over 2.5 billion years to optimize the resources available to these plants and algae, with the ability to store over 100 TW of energy annually.[22] AP is an area of interest for many researchers looking to better utilize solar energy by creating novel photocatalysts in hopes to find new clean fuel sources.[23]

Plants are able to utilize the energy from sunlight using a series of excitations, reductions, and oxidations using photosystems I and II (PSI and PSII, Figure 1.5). PSII absorbs a photon from sunlight to generate the strongly oxidizing P680+, which splits a water molecule to extract protons and electrons and one half of an oxygen molecule.[24] This initiates chemiosmosis, the transfer of protons through a semipermeable membrane, and a series of electron transfers to PSI. Along with additional photon absorption, PSI utilizes the hydrogenase enzyme to reduce cofactor nicotinamide adenine dinucleotide phosphate ($NADP^+$) to NADPH. The transfer of charges in P700 provides the energy needed to convert ADP to ATP. The ATP and the biological hydrogen, NADPH, provides electrons, hydrogen, and energy to Calvin cycle to convert CO_2 into glucose, which is a source of energy and carbon fixation within plant matter.[25]

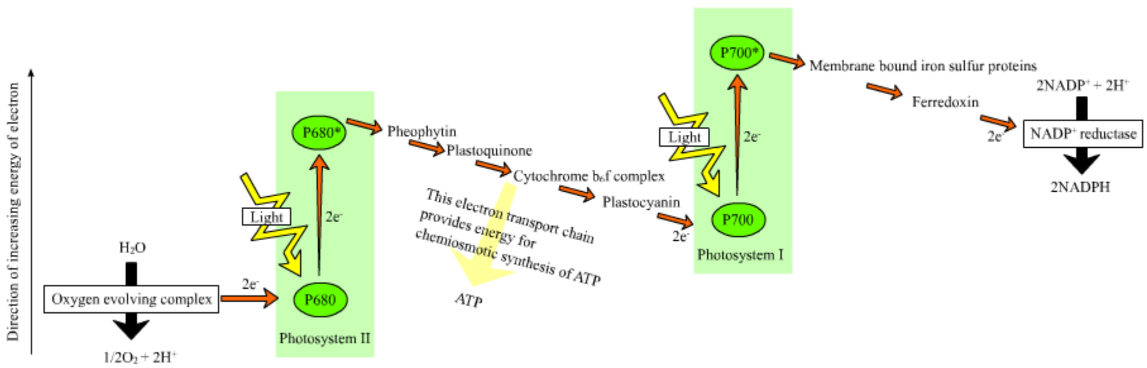

Figure 1.5. Diagram of the reaction steps in PSI and PSII.[24]

Many microorganisms, like cyanobacteria and algae, are highly efficient in photosynthetic water splitting by utilizing metal-enzymes called hydrogenases. These enzymes are responsible for water oxidation and reduction and have three general types: [NiFe]-, [FeFe]-, and [Fe]-hydrogenase. The two former utilize a dinuclear metal center with an iron and nickel or two iron active sites, and the latter employs a single iron metal center active site.[26] These hydrogenase enzymes are highly interesting to researchers as they utilize first row transition metal centers instead of precious noble metals.

For the benefit of optimizing AP catalysis, the photosynthetic process can be divided into the oxidative and reductive portions. In a more general light-initiated reaction, when a chromophore absorbs a photon, an electron is excited, generating a charge separation between the excited electron and the hole. This allows for the consideration of each of the half reactions, where the electrons participate in the reductive hydrogen evolution reaction (HER) and the holes participate in the oxygen evolution reaction (OER, Figure 1.6). Hydrogen generation is a two electron process, whereas oxygen generation requires the loss of four electrons.

$$2\ H_2O \rightarrow O_2 + 4\ H^+ + 4\ e^-$$

$$4\ H^+ + 4\ e^- \rightarrow 2\ H_2$$

Figure 1.6. Water splitting reactions

The Uses of Hydrogen

Focusing on the reductive side of AP, it is possible to generate hydrogen gas from two protons and two electrons. Hydrogen is a clean burning gas that produces only water as a byproduct, with an energy per kilogram density 2.8 greater than that of gasoline.[27] Hydrogen is used in industrial processes, like Fischer-Tropsch synthesis to generate hydrocarbon fuels from carbon monoxide and hydrogen gas[28] or the Haber-Bosch process that reacts nitrogen and hydrogen gases to create ammonia fertilizer. These industrial uses of hydrogen are highly important to modern civilization, but the ways in which the hydrogen is generated must be carefully considered.

While hydrogen is the most abundant element in the universe, making up over 75% of the universe's known mass, it does not occur in its elemental form on Earth. Rather, almost all of the hydrogen on earth is stored in water, hydrocarbons, and organic materials. Most of the hydrogen gas that is present on Earth has been made using fossil fuels via gasification and the water-gas shift reaction. This process involves the pyrolysis of organic material into carbon monoxide, which is then reacted with water to produce H_2 and CO_2.[29] This is not a sustainable method to create hydrogen gas, as it is still using the limited fossil fuel reserves, requires a vast amount of energy input to create the reactants, and emits CO_2 as a by-product.

Hydrogen is a direct source of chemical energy and can be harvested by burning hydrogen in similar systems that utilize fossil fuel combustion, or used in fuel cells by harnessing the energy released when H_2 and O_2 are combined to form water, with chemical-to-electrical energy conversion of over 60%.[30] This efficiency is much greater than compared to fossil fuels with fuel energy-to-electricity efficiencies of 32-45%.[31] It also must be considered that fossil fuels are made from biomass, which originally obtained all of its energy through photosynthesis, and plants have only a 4.5% efficiency for converting sunlight into energy.[24] It is easy to see that there is a great disparity in the energy that could be generated using sunlight and how much energy is actually converted into electricity using our current systems. A better method is needed to sustainably produce H_2 to be used as a clean and renewable energy source. For this, scientists have looked to the use of catalysts for hydrogen generation.

Developing Chemical Catalysts

Electrocatalysts

In order to determine the efficacy of a catalyst at reducing protons, there must be a standard set of tests to allow for direct comparison between catalysts. Electrochemistry is a helpful tool for investigating the transfer of electrons, and is vital for probing metal complexes for reductions and oxidations.[32] Cyclic voltammograms (CV) measure applied voltage (V) versus current (i) and are obtained when a solution of the catalyst is probed by scanning potentials cyclically with a working, reference, and counter electrode.

While the end goal is the design of a highly effective photocatalyst for HER, invaluable information can be gleaned from an electrochemical investigation into each catalyst. There are units of measure to compare efficiency and activity to examine the catalytic abilities of a complex. Overpotential is a measure of the efficiency of the catalyst, defined as the extra energy input over the thermodynamically-determined redox potential required for the reaction to occur.[33] The activity is measured by the catalytic current enhancement (i_c / i_p). When a proton source is added, an irreversible catalytic wave appears at a more negative potential than the metal redox peaks. The ratio between the current of the proton reduction peak (i_c) and the metal reduction peak (i_p) is an indication of how active a catalyst is for proton reduction. (Figure 1.7). The activity of a catalyst can also be assessed by calculating the number of catalytic reactions per unit time, defined as the turnover frequency (TOF).

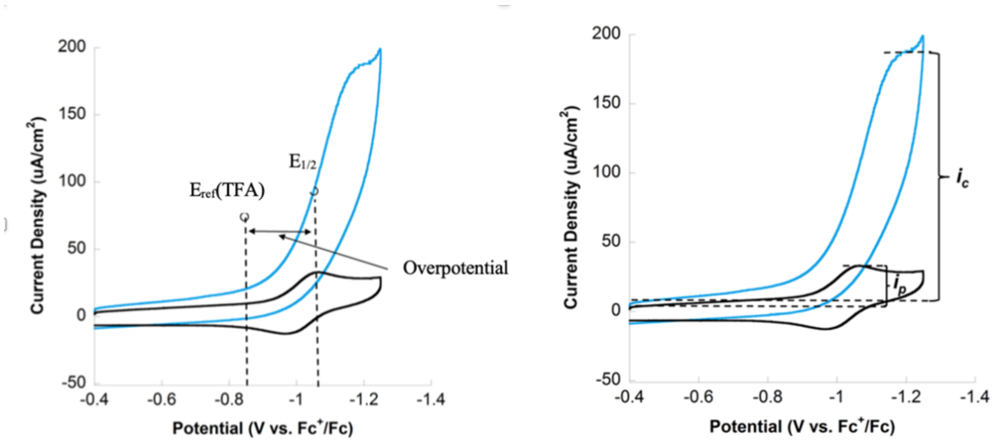

Figure 1.7. Diagram of overpotential and i_c / i_p.[34]

Platinum is a benchmark electrocatalyst for HER due to its high activity, low overpotential, and robustness.[35] This is partially due to its near-neutral free energy of adsorption of H_2, allowing for an ideal strength of bonding of hydrogen to the Pt surface: strong enough to form products, but not too strong as to not allow for the release of the produced H_2.[36,37] While Pt has been consistently found to be the most effective HER electrocatalyst, the abundance of Pt in the earth's crust presents an issue when considering the scalability of Pt catalysts. Pt is very scarce in the earth's crust, and is therefore costly and precious, making it a poor candidate for scaling up Pt catalytic systems to produce industrial amounts of hydrogen.[38]

An analysis of the abundance of metals in the earth's crust illustrates the scarcity of heavy metals in the platinum and gold family, such as iridium, palladium, and ruthenium, and an abundance of first row earth metals, such as iron and titanium (Figure 1.8). This has pushed many scientists to investigate the uses of abundantly available first row transition metals, with some looking towards nature for inspiration.

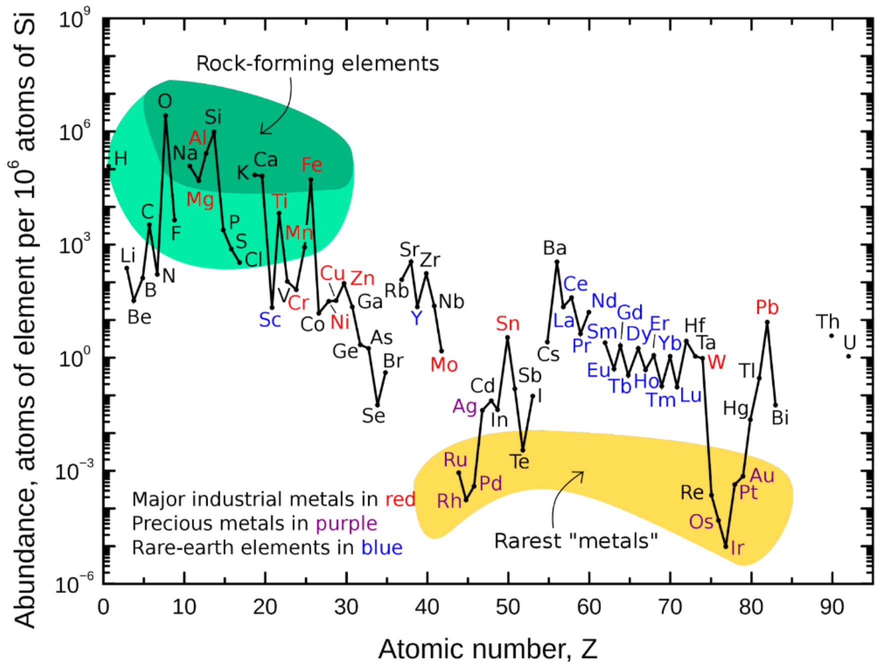

Figure 1.8. Abundance of metals on earth[39]

Researchers have successfully explored ways to incorporate earth abundant first row transition metals into electrocatalysts with hydrogenase mimics, by either taking a top-down or a bottom-up approach to synthesizing ligands and complexing with first-row transition metals. The top-down approach utilizes a biological assembly of the enzyme mimics in their natural environment, and tend to be studied for their biomimetic characteristics,[40] and the bottom-up approach results in a simpler molecule that can be assessed for its hydrogen generating catalytic abilities.

A 2011 study by Helm, et al. involved the synthesis of the Dubois catalyst modeled after the [FeFe]-hydrogenase. It was found to be a highly active electrocatalyst, achieving an i_c/i_p of 38 and turnover frequency of over 33,000 s^{-1} in acetonitrile (ACN). The electrocatalyst was found to operate at an overpotential of 625 mV with a protonated dimethylformamide proton source. The catalytic activity was increased in the presence of water, with an i_c/i_p of 74 and TOF of over 100,000 s^{-1}, explicating the catalytic ability to generate hydrogen from aqueous solutions (Figure 1.9 a).[41] The Dubois catalyst was shown to be stable in moderately acidic environments, but that isn't always the case for the hydrogenase mimics. In 2016, Xu et al. synthesized the first iron-only hydrogenase mimic that somewhat stable for catalytic hydrogenation, but is still highly susceptible to decomposition (Figure 1.9 b).[42] It is therefore more beneficial to have a looser interpretation of the hydrogenase active site to increase the possible catalytic activity. Our research group was inspired by the iron-only active site when designing the tetradentate polypyridyl monophenolate ligand complexed with an iron center to generate an iron polypyridyl complex (Figure 1.9 c). This catalyst was found to be stable in acidic and aqueous conditions, operating at an overpotential of 800 mV with an i_c/i_p of 7.8 in acetonitrile. The catalyst showed increased activity in aqueous solutions, with an i_c/i_p of 11.9 after the addition of water.[34] This catalyst is of great interest to our group and is still being investigated with modifications currently.

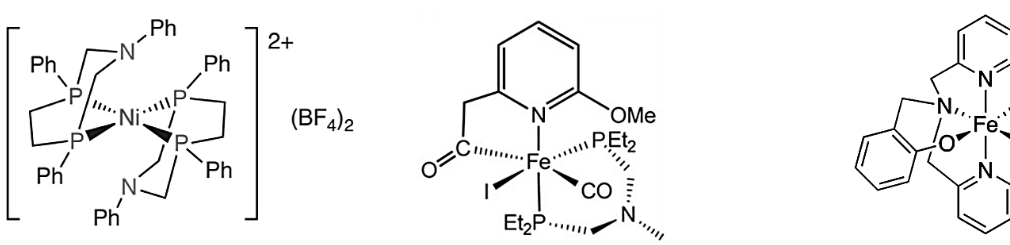

a b c

Figure 1.9. Hydrogenase inspired electrocatalysts by Helm [41] (a), Xu [42] (b) and Connor [43] (c).

Photocatalysts

While effective electrocatalysts outlined have demonstrated highly efficient hydrogen generating abilities, photocatalysts are of great importance as they can enable the use of sunlight, rather than electricity, to power hydrogen generation. Photocatalytic systems work by using a chromophore to absorb photons and excite electrons to pass to the catalyst for HER and a sacrificial electron donor to quench the chromophore (Figure 1.10). The measure of the efficiency of a photocatalyst is the turnover number (TON), which indicates the moles of H_2 produced per mole of catalyst. The rate of hydrogen generation can also be determined photocatalytically with the turnover frequency (TOF) corresponding to the moles of hydrogen generated per mole of catalyst per unit time.

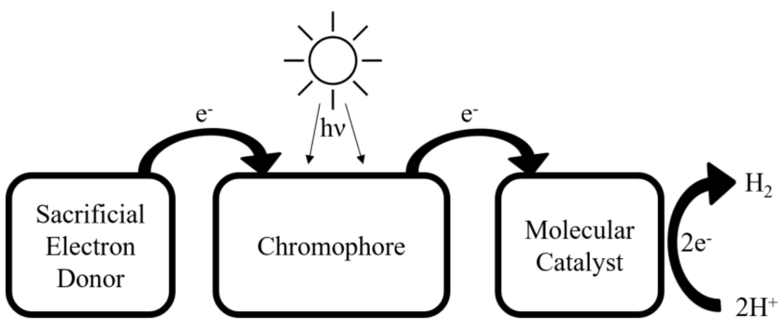

Figure 1.10. Diagram of photochemical system.

Design of a photocatalytic system includes the choice of chromophore and electron donor. Generally, each chromophore functions most efficiently in a specific protonation state, so the pH of the solution is important to the ability of the chromophore to absorb photons and transfer electrons to the catalyst. The electron donor has a large effect on the pH of the system and is chosen to best pair with the pH requirements of the chromophore. While pH can be adjusted to best suit the system, the ability of the electron donor to donate electrons is affected by the pH, so optimization may be required.

The chemical composition of the chromophore should also be considered when designing the photocatalytic system. Precious metals, such as ruthenium, have been shown to be a component of highly effective photocatalytic systems presented in work by the Eisenberg group. McNamara et al. built a photocatalytic system with a series of cobalt-dithiolene complexes with varied substituents as catalysts for HER from water by utilizing a tris(bipyridine)ruthenium(II) chloride ($Ru(bpy)_3^{2+}$) chromophore and ascorbic acid electron donor. This system operates at pH 4 in equal parts acetonitrile and water and is a highly effective photocatalytic system with the Co-dithiolene catalyst with the strongest electron withdrawing group, generating TONs of over 9,000 and TOFs of over 3,400 h^{-1}.[43] Chan et al. investigated $Ru(bpy)_3^{2+}$ with a triethanolamine (TEOA) electron donor at differing pH, and they found that the pH affected the number of bound bipyridines as well as a change in oxidation state. $Ru(bpy)_3^{2+}$ and TEOA generated the most hydrogen with a platinum catalyst but was unable to generate much hydrogen with a cobalt catalyst in pH 8.1.[44] This illustrates the catalyst, chromophore, and electron donor must all be compatible to optimize water reduction.

While ruthenium chromophores have been found to be effective at generating hydrogen under certain conditions, the availability of the precious platinum-group metal still limits the ability to scale up these systems in a cost-effective manner. Luminescent metal-free organic dyes, such as xanthenes

(Figure 1.11), are a promising alternative to precious metal chromophores and have been found to be effective in photocatalytic systems.[45]

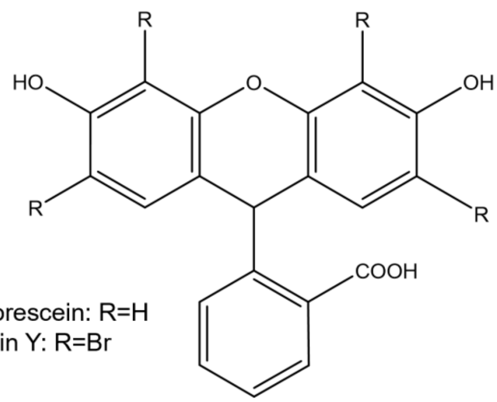

Fluorescein: R=H
Eosin Y: R=Br

Figure 1.11. Structure of xanthene, with R=H for fluorescein and R=Br for Eosin Y

Motz et al. reported a photocatalytic system with the organic dye, Eosin Y, and TEOA electron donor to investigate a series of cobaloxime derivatives as water reduction catalysts. They determined that the system was suitable for hydrogen generation, and the best cobaloxime derivative for water reductions were those that have high hydride affinity and redox-active ligands that are able to hydrogen bond, promoting the availability of hydrogen near the active site of the catalyst resulting in water reduction.[46]

Wang et al. also reported a successful Eosin Y and TEOA system for water reduction by a binuclear cobalt catalyst, and pH studies determined maximum hydrogen generation in pH 8 conditions, with overall better hydrogen generation in more basic versus acidic environments. This may be attributed to the protonation state of the TEOA, further exemplifying that the pH of the system must be suitable for the chromophore and electron donor. TONs of over 1000 were reported when utilizing a system of 4.0 x 10-4 M Eosin Y and 5% TEOA in a 3:1 acetonitrile to water ratio.[47]

Fluorescein (Fl) is another xanthene derivative organic dye that has been studied for use in photocatalytic water reduction systems. Eisenberg's research group in 2012 designed a noble-metal free photocatalytic system for hydrogen generation from 1:1 ethanol: water with a fluorescein chromophore, TEA electron donor, and nickel thiolate catalyst. The system generated over 5500 TON over 40 hours, and was stable for over 60 hours.[48] These findings were highly significant at the time, as no other organic dye system was able to generate hydrogen for longer than a few hours. Quenching studies revealed that system longevity could be attributed to oxidative quenching of the Fl chromophore in lower concentrations of TEA, with TEA donating electrons after Fl donates electrons needed for catalysis (Figure 1.12).

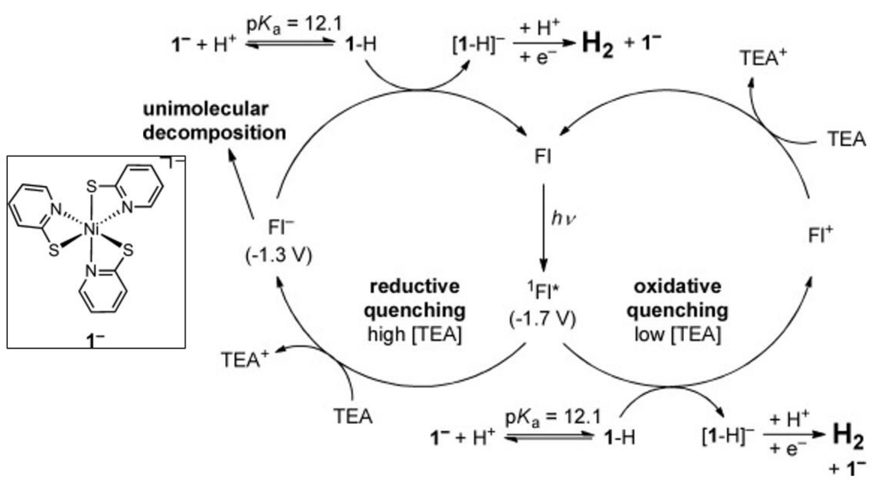

Figure 1.12. Structure of nickel catalyst and diagram of quenching pathways.[48]

Since this work, our research group has had great success with Fl chromophores paired with TEA electron donor. A 2015 study with nickel bis-dithiocarbazate Schiff base catalyst was found to generate over 3300 TONs in a highly stable system lasting over 70 hours with a Fl chromophore and TEA electron donor.[49] Quenching studies concur with the previous Eisenburg study, finding that both oxidative and reductive quenching pathways were possible with Fl. Low TEA concentrations coincided with oxidative quenching and a greater stability of the Fl and catalyst system, and TEA was found to be the limiting factor in the oxidative pathway. The researchers also propose static quenching as a possible Fl quenching mechanism, where π-stacking between the Fl chromophore and catalyst allows for non-diffusion based electron transfer. It was proposed that this static oxidative quenching may contribute to the longevity of the system.

Heterogeneous and homogeneous catalysts

Since the discovery of solar water splitting using TiO_2 by Honda and Fujishima in the 1970's,[50] there has been a push to optimize the use of TiO_2 as a heterogeneous photocatalyst for water splitting. TiO_2 is a promising component of a catalytic system because it is stable, cost-effective, non-corrosive, non-toxic, and abundantly available. However, TiO_2 is not an effective catalyst alone due to electron-hole recombination and large band gap corresponding to higher energy UV absorption. Electron-hole recombination is detrimental because the photoexcited electron does not transfer to the catalyst to be utilized in water reduction but instead falls back to the lower energy valence band and recombines with the hole to release energy in the form of heat or light. The greater than 3 eV band gap requires higher energy UV photons for excitation from the VB to CB. However, UV light makes up only 8% of the sunlight that reaches the earth's surface, whereas visible light makes up over 42%.[51]

Modifications can be made to TiO_2 to improve its ability to absorb light in the visible spectrum. Dye sensitization, via adsorption or covalent bonding of a dye onto the surface of TiO_2, allows for charge transfer from the photoexcited dye into the CB of the TiO_2.[52] This widens the range of light able to be absorbed by the photocatalytic system, allowing the absorption of more abundant visible light, and therefore making the system more efficient at absorbing sunlight.

TiO_2 has two main morphologies: anatase with a 3.2 eV band gap and rutile with a 3.0 eV band gap. Pure anatase has been found to be more photochemically active, but a combination of the two morphologies has been found to be more active than the pure form of either anatase or rutile.[53] This may be due to doping or junction effects of the semiconductors with differing band gaps, increasing activity and ability to make the most out of sunlight, similar to effects found in bulk phase semiconductors used in PV systems.

Charge transfer can also occur out of the TiO_2 to an immobilized catalyst to provide the reductive potential required for hydrogen generation and lower the occurrence of electron-hole recombination (Figure 1.13). Hirano et al. designed a water reduction photocatalytic system using P25 TiO_2, which contains TiO_2 nanoparticles (NP) ranging from 10-40 nm with both anatase and rutile morphologies. Platinum NP catalyst and a $Ru(bpy)_3^{2+}$ chromophore were used with an EDTA electron donor in water. This system generated hydrogen in the presence of the catalyst supported on TiO_2 NPs, chromophore, and electron donor, but produced little to no hydrogen in the absence of either catalyst, TiO_2, or chromophore, indicating that all components were necessary for a successful photocatalytic system.[54]

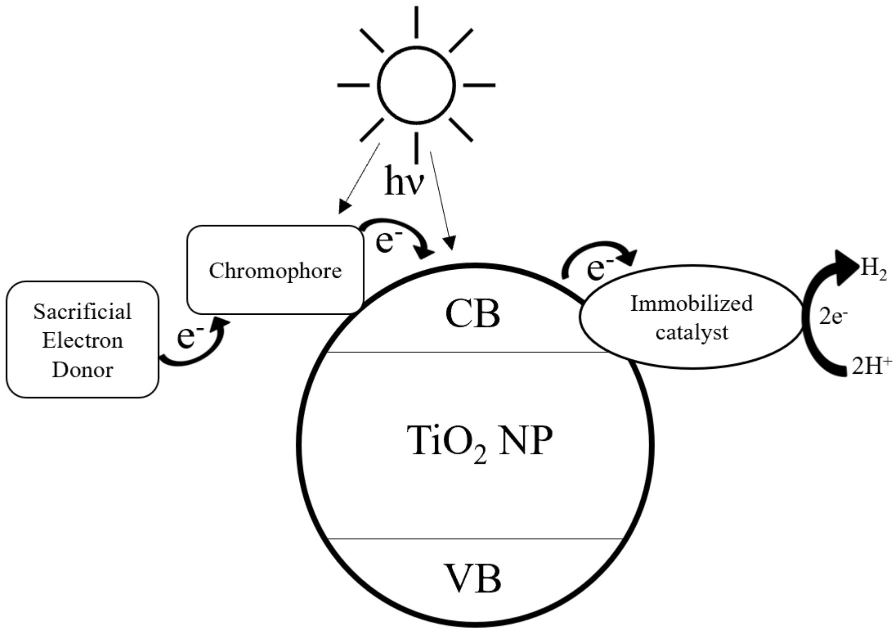

Figure 1.13. Diagram of a photocatalytic system with TiO_2 nanoparticle.

TiO_2 NP photocatalytic systems without a precious metal catalyst have also been reported. In 2011, Reisner et al. reported a cobalt catalyst functionalized with a phosphonic acid anchoring group supported on TiO_2 NP with $Ru(bpy)_3^{2+}$ chromophore, which was also functionalized and immobilized with phosphonic acid anchoring group, and TEOA electron donor. The system was not found to be very stable, as it ceased H_2 generation after 8 hours with TONs of 53, but it serves as an important proof of concept for noble-metal free catalysts and TiO_2 heterogeneous systems.[55] In 2014, Yin et al. described an entirely noble metal-free system with a carboxylate-functionalized cobalt catalyst covalently bound to TiO_2 NPs with eosin y chromophore and TEA electron donor.[56] This system was marginally more stable, with TONs of 90 over 6 hours, but exemplified the ability to create TiO_2 NP based systems without precious metals to generate hydrogen.

In the investigation into first row transition metal catalysts, the most abundant metal, iron, has not been as thoroughly explored as cobalt or nickel.[25] In addition, many [Fe]-hydrogenase mimics employ the use of precious metal chromophores for water reduction instead of more cost-effective organic dye chromophores.[57] Our group has investigated the use of an iron center in a [Fe]-hydrogenase-inspired family of catalysts. As discussed previously with the electrocatalysts, the iron polypyridyl catalyst was shown to be effective at reducing protons in organic and aqueous mediums. When introduced into a homogeneous photocatalytic system, the iron polypyridyl complex produced TONs of over 2000 in a Fl and TEA system.[58] The catalyst was later incorporated into a heterogeneous system by immobilizing the catalyst on TiO_2 NP using a phosphonic acid anchor.[59] This shift from homogeneous to heterogeneous TiO_2 system increased the TONs to over 7,800. This illustrates the benefit that can be gained by incorporating semiconductors into photocatalytic systems.

Homogeneous Catalysts:

Although these heterogeneous photocatalytic systems have been an important proof of principle study to exemplify how hydrogen can be generated from water using the power of the sun, it is still important to find new catalysts for hydrogen generation that are active and cost effective. Therefore, studies into finding novel molecular catalysts that are economically and environmentally viable are necessary. When beginning the search for new catalysts, investigating molecular catalysts is a good starting point. While molecular catalysts are not always as effective at generating hydrogen as some heterogeneous catalysts, there are key advantages that bolster their usefulness and need to be researched. Molecular catalysts are able to be more fully understood in regards to its exact structure, specific active sites, and catalytic mechanisms.[60]

As stated previously, the choice of metal for the catalyst's active site should be carefully considered. While precious metals have been shown to be highly effective at catalyzing HER, the need to be able to scale up photocatalytic systems for wide spread or industrial use renders precious metals economically restricting. Many examples have been provided of a more economically viable option to utilize earth abundant first row transition metals, and many improvements have been made to improve the effectiveness of these catalysts over the past few decades.

Apart from the choice of metal in designing a catalyst, much attention must be paid to the ligands which will be coordinated to the metal center. The ligand's structure and chemical composition allows for tunability of the coordination environment around the metal center and adjustments in redox potentials.[26] The ligands can affect the acidity of the metal hydride once the initial proton has coordinated with the active metal site, as the transfer of a proton to and from an active site can be inhibitory to proton reduction. The acidity can be altered by the ligand choice, as an electron withdrawing ligand can form a metal hydride complex with a lower pKa than that of a metal hydride complex with a more electron donating ligand.[61] This can allow the complex to be more readily reduced and may lower the reduction potential needed for the complex to catalyze hydrogen. A 2016 study from the Hartley et al. found that functionalizing an iron polypyridyl catalyst with an electron-withdrawing nitro group resulted in a 300 mV overpotential, which corresponds to a 500 mV overpotential improvement over the parent catalyst.[62]

The binding of the ligand can alter the stability of a metal complex. Multi-dentate ligands have increased stability due to the chelate effect. Formation of complexes with multidentate, rather than monodentate, ligands are more thermodynamically stable, tend to have fewer steric hindrances and dipole interactions between ligands, and have the opportunity to have more aromatic character, with which ligand-metal π bonding can produce resonance stabilization through further delocalization of electrons.[63]

Another aspect to consider is the innocence of the ligand. Redox active ligands have shown useful for water splitting catalysts. For two electron processes, like water reduction, heavier metals allow for the transfer of two electrons due to the greater number of oxidation states available to the heavier metal. Lighter metals, such as Co or Fe, have fewer oxidation states and are more likely to engage in single-electron processes. While concurrent electron transfers can allow for the proper number of electrons for a multi-electron process to occur, radical intermediates are common after the primary electron transfer and may result in undesired reactions occurring. Redox-active ligands may be reduced concurrently with the metal and can allow for two electrons to transfer simultaneously without the risk for intermediate undesired reactions.[64]

Molecular catalysts require diffusion-based kinetics to interact with the electron source, as there are no bonds attaching the catalyst to the chromophore. Ligand design can modify this aspect as shown by research by Wang et al in 2022.[65] They utilized π-stacking to facilitate electron transfer from the chromophore to the catalyst and found an increase in quantum yield and reaction selectivity. While the electron transfer was not as great as what occurred with covalent linking between the chromophore and catalyst, it was found to decrease charge recombination, which can be detrimental to the catalytic activity.

A great benefit of beginning catalyst design in the molecular stage is the ability to tune and characterize the structure of the catalyst, and then immobilize the molecules onto heterogeneous structures, such as carbonaceous materials or metal-oxide semiconductors to alter reaction processes. Previous research has been done on complex functionalization and immobilization in our lab. The parent complex (Figure 1.14 a) was functionalized with a naphthalene (Figure 1.14 b) adsorbed onto carbon surfaces with π-stacking. It was found that the catalyst successfully adsorbed on a glassy carbon surface and resulted in improved overpotential of the electrocatalyst.[66] A phosphonic acid anchoring group (Figure 1.14 c) was also investigated for covalent bonding onto metal-oxide surfaces. This incorporation of a molecular catalyst into a heterogeneous system allowed for a 3.5-fold improvement in TON under photocatalytic conditions.[59] This is an important proof of concept that active molecular catalysts can be improved upon by incorporation into heterogeneous systems, and displays great promise for catalyst design.

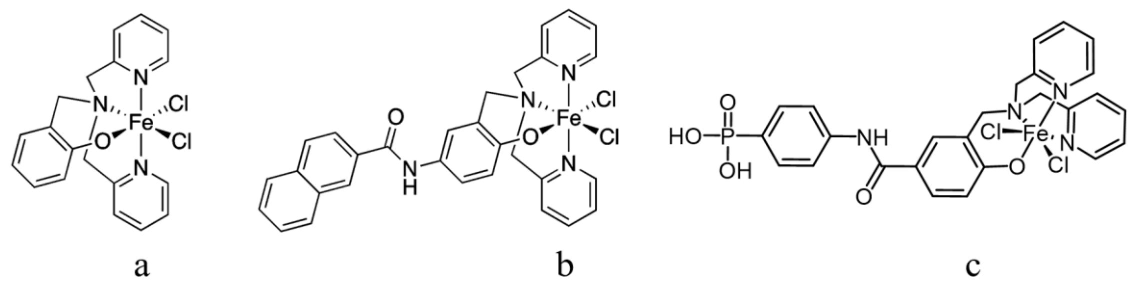

Figure 1.14. Parent iron polypyridyl catalyst (a) with naphthalene functionalization[66] (b) and phosphonic acid functionalization[59] (c).

Natural Water Sources for Hydrogen Generation

An important focus of this research has been investigating catalytic ability to reduce water from impure systems. If photocatalysts are to be widely used for generating hydrogen around the world, or possibly on other planets, it is necessary to assess the robustness of the catalyst. To do so, natural water sources have been investigated.

Previous research in our group has shown that the iron polypyridyl catalyst is effective for HER in water obtained from Lake Matoaka on the William & Mary campus with a two-fold reduction of TONs.[58] This inspired the investigation into the most prevalent water source, sea water (Figure 1.15). As saltwater makes up over 97% of the water present on Earth,[67] it is of vital importance to utilize this water to generate hydrogen gas. As pure water becomes more scarce throughout the world, this ability to generate hydrogen from saltwater would allow for the generation of pure water when the hydrogen generated is used in fuel cells. The Apollo 11 mission to the moon in 1969 utilized this technology, as the command center was powered by a hydrogen fuel cell, and the crew drank the water from the fuel cell for the duration of the space flight.[68] This shows the impact that a robust photocatalyst could have on the future of energy and water purification.

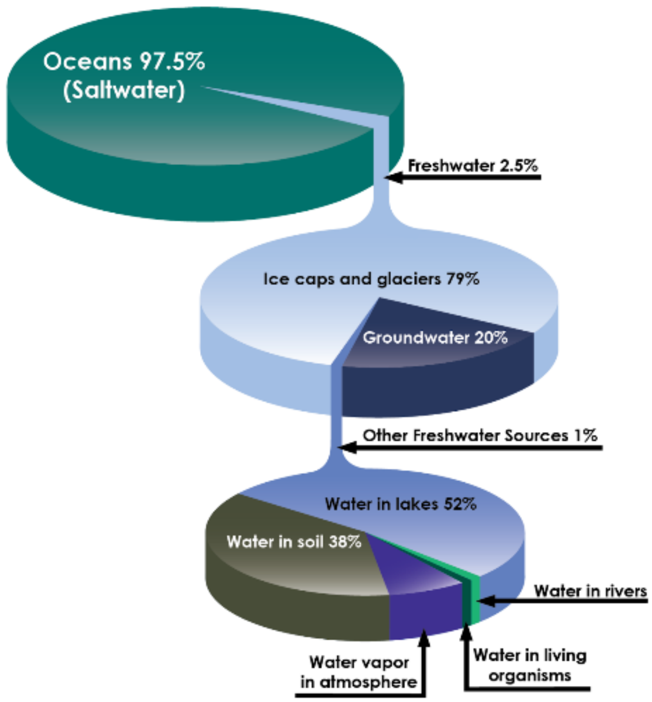

Figure 1.15. Diagram of saltwater and freshwater distribution on earth.[67]

References:

1. *World Population by Year - Worldometer*. https://www.worldometers.info/world-population/world-population-by-year/ (accessed 2023-03-31).
2. *Fossil fuel sources accounted for 79% of U.S. consumption of primary energy in 2021*. https://www.eia.gov/todayinenergy/detail.php?id=52959 (accessed 2023-04-02).
3. *EIA projects nearly 50% increase in world energy usage by 2050, led by growth in Asia*. https://www.eia.gov/todayinenergy/detail.php?id=41433 (accessed 2023-04-02).
4. Lewis, N. S.; Nocera, D. G. Powering the Planet: Chemical Challenges in Solar Energy Utilization. *Proc. Natl. Acad. Sci.* **2006**, *103* (43), 15729–15735. https://doi.org/10.1073/pnas.0603395103.
5. Vohra, K.; Vodonos, A.; Schwartz, J.; Marais, E. A.; Sulprizio, M. P.; Mickley, L. J. Global Mortality from Outdoor Fine Particle Pollution Generated by Fossil Fuel Combustion: Results from GEOS-Chem. *Environ. Res.* **2021**, *195*, 110754. https://doi.org/10.1016/j.envres.2021.110754.
6. *Climate Change: Atmospheric Carbon Dioxide | NOAA Climate.gov*. http://www.climate.gov/news-features/understanding-climate/climate-change-atmospheric-carbon-dioxide (accessed 2023-04-02).
7. Treut, H. L.; Somerville, R.; Cubasch, U.; Ding, Y.; Mauritzen, C.; Mokssit, A.; Peterson, T.; Prather, M.; Allen, M.; Auer, I.; Biercamp, J.; Covey, C.; Fleming, J. R.; García-Herrera, R.; Gleckler, P.; Haigh, J.; Hegerl, G. C.; Isaksen, K.; Jones, J.; Luterbacher, J.; MacCracken, M.; Penner, J. E.; Pfister, C.; Roeckner, E.; Santer, B.; Schott, F.; Sirocko, F.; Staniforth, A.; Stocker, T. F.; Stouffer, R. J.; Taylor, K. E.; Trenberth, K. E.; Weisheimer, A.; Widmann, M.; Baede, A.; Griggs, D.; Treut, L.; Somerville, R.; Cubasch, U.; Ding, Y.; Mauritzen, C.; Mokssit, A.; Peterson, T.; Prather, M. Historical Overview of Climate Change Science.
8. *Ocean Acidification*. https://www.whoi.edu/. https://www.whoi.edu/know-your-ocean/ocean-topics/how-the-ocean-works/ocean-chemistry/ocean-acidification/ (accessed 2023-04-02).
9. *Coral reef ecosystems*. https://www.noaa.gov/education/resource-collections/marine-life/coral-reef-ecosystems (accessed 2023-04-02).
10. *How do coral reefs protect lives and property?* https://oceanservice.noaa.gov/facts/coral_protect.html (accessed 2023-04-02).
11. *IPCC_AR6_WGII_SummaryForPolicymakers.pdf*. https://www.ipcc.ch/report/ar6/wg2/downloads/report/IPCC_AR6_WGII_SummaryForPolicymakers.pdf (accessed 2023-04-02).
12. *Increasing renewables likely to reduce coal and natural gas generation over next two years*. https://www.eia.gov/todayinenergy/detail.php?id=55239 (accessed 2023-02-20).
13. *Wind energy*. https://www.irena.org/Energy-Transition/Technology/Wind-energy (accessed 2023-04-04).
14. *Advantages and Challenges of Wind Energy*. Energy.gov. https://www.energy.gov/eere/wind/advantages-and-challenges-wind-energy (accessed 2023-04-04).

15. US EPA, O. *Solar Heating and Cooling Technologies*. https://www.epa.gov/rhc/solar-heating-and-cooling-technologies (accessed 2023-04-04).
16. *Photovoltaics and electricity - U.S. Energy Information Administration (EIA)*. https://www.eia.gov/energyexplained/solar/photovoltaics-and-electricity.php (accessed 2023-04-04).
17. *Joshua Halpern and Scott Johnson*. Chemistry 2000. https://chem.libretexts.org/Courses/Prince_Georges_Community_College/CHEM_2000%3A_Chemistry_for_Engineers_(Sinex)/Unit_3%3A_States_of_Matter/Chapter_8%3A_Solids/Chapter_12.06%3A_Metals_and_Semiconductors (accessed 2023-04-04).
18. *Photovoltaic Energy Factsheet*. Center for Sustainable Systems. https://css.umich.edu/publications/factsheets/energy/photovoltaic-energy-factsheet (accessed 2023-04-04).
19. *Solar Photovoltaic Cell Basics*. Energy.gov. https://www.energy.gov/eere/solar/solar-photovoltaic-cell-basics (accessed 2023-04-02).
20. *More than half of new U.S. electric-generating capacity in 2023 will be solar*. https://www.eia.gov/todayinenergy/detail.php?id=55419 (accessed 2023-04-04).
21. *Photosynthetic light harvesting: excitons and coherence | Journal of The Royal Society Interface*. https://royalsocietypublishing.org/doi/10.1098/rsif.2013.0901 (accessed 2023-04-02).
22. Barber, J. Biological Solar Energy. *Philos. Trans. R. Soc. Math. Phys. Eng. Sci.* **2007**, *365* (1853), 1007–1023. https://doi.org/10.1098/rsta.2006.1962.
23. Nocera, D. G. The Artificial Leaf. *Acc. Chem. Res.* **2012**, *45* (5), 767–776. https://doi.org/10.1021/ar2003013.
24. Barber, J.; Tran, P. D. From Natural to Artificial Photosynthesis. *J. R. Soc. Interface* **2013**, *10* (81), 20120984. https://doi.org/10.1098/rsif.2012.0984.
25. Du, P.; Eisenberg, R. Catalysts Made of Earth-Abundant Elements (Co, Ni, Fe) for Water Splitting: Recent Progress and Future Challenges. *Energy Environ. Sci.* **2012**, *5* (3), 6012–6021. https://doi.org/10.1039/C2EE03250C.
26. Tran, P. D.; Artero, V.; Fontecave, M. Water Electrolysis and Photoelectrolysis on Electrodes Engineered Using Biological and Bio-Inspired Molecular Systems. *Energy Environ. Sci.* **2010**, *3* (6), 727–747. https://doi.org/10.1039/B926749B.
27. *Hydrogen Fuel Basics*. Energy.gov. https://www.energy.gov/eere/fuelcells/hydrogen-fuel-basics (accessed 2023-03-31).
28. *10.2. Fischer-Tropsch Synthesis*. netl.doe.gov. https://netl.doe.gov/research/carbon-management/energy-systems/gasification/gasifipedia/ftsynthesis (accessed 2023-04-03).
29. *Hydrogen Production: Biomass Gasification*. Energy.gov. https://www.energy.gov/eere/fuelcells/hydrogen-production-biomass-gasification (accessed 2023-03-31).

30. *Fuel Cells*. Energy.gov. https://www.energy.gov/eere/fuelcells/fuel-cells (accessed 2023-03-31).
31. More than 60% of Energy Used for Electricity Generation Is Lost in Conversion. https://www.eia.gov/todayinenergy/detail.php?id=44436 (accessed 2023-02-20).
32. Elgrishi, N.; Rountree, K. J.; McCarthy, B. D.; Rountree, E. S.; Eisenhart, T. T.; Dempsey, J. L. A Practical Beginner's Guide to Cyclic Voltammetry. *J. Chem. Educ.* **2018**, *95* (2), 197–206. https://doi.org/10.1021/acs.jchemed.7b00361.
33. Appel, A. M.; Helm, M. L. Determining the Overpotential for a Molecular Electrocatalyst. *ACS Catal.* **2014**, *4* (2), 630–633. https://doi.org/10.1021/cs401013v.
34. Connor, G. P.; Mayer, K. J.; Tribble, C. S.; McNamara, W. R. Hydrogen Evolution Catalyzed by an Iron Polypyridyl Complex in Aqueous Solutions. *Inorg. Chem.* **2014**, *53* (11), 5408–5410. https://doi.org/10.1021/ic500069c.
35. McCrory, C. C. L.; Jung, S.; Ferrer, I. M.; Chatman, S. M.; Peters, J. C.; Jaramillo, T. F. Benchmarking Hydrogen Evolving Reaction and Oxygen Evolving Reaction Electrocatalysts for Solar Water Splitting Devices. *J. Am. Chem. Soc.* **2015**, *137* (13), 4347–4357. https://doi.org/10.1021/ja510442p.
36. *A Challenge to the G ∼ 0 Interpretation of Hydrogen Evolution* | *ACS Catalysis*. https://pubs.acs.org/doi/10.1021/acscatal.9b02799 (accessed 2023-04-05).
37. Nørskov, J. K.; Bligaard, T.; Logadottir, A.; Kitchin, J. R.; Chen, J. G.; Pandelov, S.; Stimming, U. Trends in the Exchange Current for Hydrogen Evolution. *J. Electrochem. Soc.* **2005**, *152* (3), J23. https://doi.org/10.1149/1.1856988.
38. Vesborg, P. C. K.; Jaramillo, T. F. Addressing the Terawatt Challenge: Scalability in the Supply of Chemical Elements for Renewable Energy. *RSC Adv.* **2012**, *2* (21), 7933–7947. https://doi.org/10.1039/C2RA20839C.
39. Abundance of Elements in Earth's Crust. *Wikipedia*; 2023.
40. Kleinhaus, J. T.; Wittkamp, F.; Yadav, S.; Siegmund, D.; Apfel, U.-P. [FeFe]-Hydrogenases: Maturation and Reactivity of Enzymatic Systems and Overview of Biomimetic Models. *Chem. Soc. Rev.* **2021**, *50* (3), 1668–1784. https://doi.org/10.1039/D0CS01089H.
41. Helm, M. L.; Stewart, M. P.; Bullock, R. M.; DuBois, M. R.; DuBois, D. L. A Synthetic Nickel Electrocatalyst with a Turnover Frequency Above 100,000 S−1 for H2 Production. *Science* **2011**, *333* (6044), 863–866. https://doi.org/10.1126/science.1205864.
42. *A Functional Model of [Fe]-Hydrogenase* | *Journal of the American Chemical Society*. https://pubs.acs.org/doi/10.1021/jacs.5b12095 (accessed 2023-04-05).
43. McNamara, W. R.; Han, Z.; Yin, C.-J. (Madeline); Brennessel, W. W.; Holland, P. L.; Eisenberg, R. Cobalt-Dithiolene Complexes for the Photocatalytic and Electrocatalytic Reduction of Protons in Aqueous Solutions. *Proc. Natl. Acad. Sci.* **2012**, *109* (39), 15594–15599. https://doi.org/10.1073/pnas.1120757109.
44. Chan, S.-F.; Chou, M.; Creutz, C.; Matsubara, T.; Sutin, N. Mechanism of the Formation of Dihydrogen from the Photoinduced Reactions of

Poly(Pyridine)Ruthenium(II) and Poly(Pyridine)Rhodium(III) Complexes. *J. Am. Chem. Soc.* **1981**, *103* (2), 369–379. https://doi.org/10.1021/ja00392a022.
45. Esswein, A. J.; Nocera, D. G. Hydrogen Production by Molecular Photocatalysis. *Chem. Rev.* **2007**, *107* (10), 4022–4047. https://doi.org/10.1021/cr050193e.
46. *High-Throughput Screening of Earth-Abundant Water Reduction Catalysts toward Photocatalytic Hydrogen Evolution* | *Inorganic Chemistry*. https://pubs.acs.org/doi/10.1021/acs.inorgchem.0c02790 (accessed 2023-04-05).
47. Wang, Z.-Y.; Rao, H.; Deng, M.-F.; Fan, Y.-T.; Hou, H.-W. Photocatalytic H2 Generation Based on Noble-Metal-Free Binuclear Cobalt Complexes Using Visible-Light. *Phys. Chem. Chem. Phys.* **2013**, *15* (39), 16665–16671. https://doi.org/10.1039/C3CP51550H.
48. Han, Z.; McNamara, W. R.; Eum, M.-S.; Holland, P. L.; Eisenberg, R. A Nickel Thiolate Catalyst for the Long-Lived Photocatalytic Production of Hydrogen in a Noble-Metal-Free System. *Angew. Chem. Int. Ed.* **2012**, *51* (7), 1667–1670. https://doi.org/10.1002/anie.201107329.
49. Wise, C. F.; Liu, D.; Mayer, K. J.; Crossland, P. M.; Hartley, C. L.; McNamara, W. R. A Nickel Complex of a Conjugated Bis-Dithiocarbazate Schiff Base for the Photocatalytic Production of Hydrogen. *Dalton Trans.* **2015**, *44* (32), 14265–14271. https://doi.org/10.1039/C5DT02042E.
50. Fujishima, A.; Honda, K. Electrochemical Photolysis of Water at a Semiconductor Electrode. *Nature* **1972**, *238* (5358), 37–38. https://doi.org/10.1038/238037a0.
51. *Solar Radiation & Photosynthetically Active Radiation*. Environmental Measurement Systems. https://www.fondriest.com/environmental-measurements/parameters/weather/photosynthetically-active-radiation/ (accessed 2023-04-05).
52. Linsebigler, A. L.; Lu, G.; Yates, J. T. Photocatalysis on TiO2 Surfaces: Principles, Mechanisms, and Selected Results. *Chem. Rev.* **1995**, *95* (3), 735–758. https://doi.org/10.1021/cr00035a013.
53. Luttrell, T.; Halpegamage, S.; Tao, J.; Kramer, A.; Sutter, E.; Batzill, M. Why Is Anatase a Better Photocatalyst than Rutile? - Model Studies on Epitaxial TiO2 Films. *Sci. Rep.* **2014**, *4* (1), 4043. https://doi.org/10.1038/srep04043.
54. Hirano, K.; Suzuki, E.; Ishikawa, A.; Moroi, T.; Shiroishi, H.; Kaneko, M. Sensitization of TiO2 Particles by Dyes to Achieve H2 Evolution by Visible Light. *J. Photochem. Photobiol. Chem.* **2000**, *136* (3), 157–161. https://doi.org/10.1016/S1010-6030(00)00342-7.
55. Lakadamyali, F.; Reisner, E. Photocatalytic H2 Evolution from Neutral Water with a Molecular Cobalt Catalyst on a Dye-Sensitised TiO2 Nanoparticle. *Chem. Commun.* **2011**, *47* (6), 1695–1697. https://doi.org/10.1039/C0CC04658B.
56. Yin, M.; Ma, S.; Wu, C.; Fan, Y. A Noble-Metal-Free Photocatalytic Hydrogen Production System Based on Cobalt(III) Complex and Eosin Y-Sensitized TiO2. *RSC Adv.* **2014**, *5* (3), 1852–1858. https://doi.org/10.1039/C4RA10767E.

57. Sun, L.; Åkermark, B.; Ott, S. Iron Hydrogenase Active Site Mimics in Supramolecular Systems Aiming for Light-Driven Hydrogen Production. *Coord. Chem. Rev.* **2005**, *249* (15), 1653–1663. https://doi.org/10.1016/j.ccr.2005.01.013.
58. Hartley, C. L.; DiRisio, R. J.; Screen, M. E.; Mayer, K. J.; McNamara, W. R. Iron Polypyridyl Complexes for Photocatalytic Hydrogen Generation. *Inorg. Chem.* **2016**, *55* (17), 8865–8870. https://doi.org/10.1021/acs.inorgchem.6b01413.
59. Race, N. A.; Zhang, W.; Screen, M. E.; Barden, B. A.; McNamara, W. R. Iron Polypyridyl Catalysts Assembled on Metal Oxide Semiconductors for Photocatalytic Hydrogen Generation. *Chem. Commun.* **2018**, *54* (26), 3290–3293. https://doi.org/10.1039/C8CC00453F.
60. Zhang, B.; Sun, L. Artificial Photosynthesis: Opportunities and Challenges of Molecular Catalysts. *Chem. Soc. Rev.* **2019**, *48* (7), 2216–2264. https://doi.org/10.1039/C8CS00897C.
61. Bullock, R. M.; Appel, A. M.; Helm, M. L. Production of Hydrogen by Electrocatalysis: Making the H–H Bond by Combining Protons and Hydrides. *Chem. Commun.* **2014**, *50* (24), 3125–3143. https://doi.org/10.1039/C3CC46135A.
62. Hartley, C. L.; DiRisio, R. J.; Chang, T. Y.; Zhang, W.; McNamara, W. R. Electrocatalytic Hydrogen Evolution by an Iron Complex Containing a Nitro-Functionalized Polypyridyl Ligand. *Polyhedron* **2016**, *114*, 133–137. https://doi.org/10.1016/j.poly.2015.11.023.
63. Huheey, J. E.; Keiter, E. A.; Keiter, R. L. *Inorganic Chemistry: Principles of Structure and Reactivity*, Fourth.
64. Luca, O. R.; Crabtree, R. H. Redox-Active Ligands in Catalysis. *Chem. Soc. Rev.* **2013**, *42* (4), 1440–1459. https://doi.org/10.1039/C2CS35228A.
65. *Co-facial π–π Interaction Expedites Sensitizer-to-Catalyst Electron Transfer for High-Performance CO2 Photoreduction* | *JACS Au*. https://pubs.acs.org/doi/10.1021/jacsau.2c00073 (accessed 2023-04-05).
66. Margonis, C. M.; Ho, M.; Travis, B. D.; Brennessel, W. W.; McNamara, W. R. Iron Polypyridyl Complex Adsorbed on Carbon Surfaces for Hydrogen Generation. *Chem. Commun.* **2021**, *57* (62), 7697–7700. https://doi.org/10.1039/D1CC02131A.
67. *Salt Water and Freshwater Distribution on Earth*. PBS LearningMedia. https://www.pbslearningmedia.org/resource/buac17-35-sci-ess-waterdistribute/saltwater-and-freshwater-distribution-on-earth/ (accessed 2023-04-05).
68. Hall, E. *Powering Apollo 11: the fuel cell that took us to the moon*. https://www.ceb.cam.ac.uk/news/powering-apollo-11-fuel-cell-took-us-moon (accessed 2023-03-31).

Chapter 2. The Synthesis, Characterization, and Electro- and Photochemical Investigation of an Iron Polypyridyl Complex Immobilized on TiO_2 Nanoparticles

Introduction

Complexes mimicking hydrogenases have been found to be successful catalysts for hydrogen generation, and while Ni and Co complexes have been extensively studied, complexes utilizing the most available and cost-effective transition metal, Fe, are lacking.[1] This was the inspiration for our group's investigation into an iron polypyridyl complex modeled after [Fe]-hydrogenase. Connor et al. reported an active electrocatalyst, **[$FeCl_2$(L)]**, with an i_c/i_p of 7.8 and overpotential of 800 mV in ACN, with increasing catalytic activity in 1:1 ACN to water with an i_c/i_p of 11.9 (Figure 2.1.a).[2] Modifications to this parent complex were made by the addition of a sulfinato group or a nitro group. Increased catalytic activity found for the sulfinato-functionalized complex with an i_c/i_p increasing to 13 and an unchanged overpotential of 800 mV, with increased activity likely due to the hemilabile nature of the sulfinato ligand (Figure 2.1.b).[3] The nitro-functionalized complex (Figure 2.1.c) was found to decrease in catalytic activity, operating at an i_c/i_p of 5.3, but found to have a 500 mV improvement for overpotential, making hydrogen generation more thermodynamically favorable. This is likely due to the electron-withdrawing nature of the nitro group.[4]

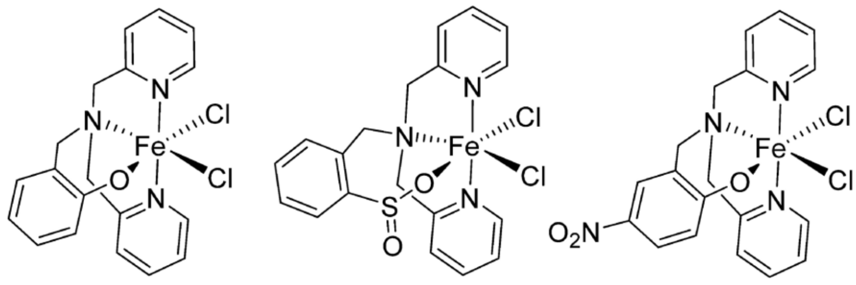

Figure 2.1. Iron polypyridyl parent complex, **$[FeCl_2(L)]$,[2]** (a), sulfinato-functionalized complex[3] (b), and nitro-functionalized complex[4] (c).

All three complexes were found to be effective for photocatalytic hydrogen generation in a 1:1 water: ethanol solution with fluorescein chromophore and TEA electron donor at a pH of 12.5. Other chromophore and electron donor pairings were tested, including $Ru(bpy)_3^{2+}$ with ascorbic acid at pH 4 and eosin Y and TEOA at pH 7, but the fluorescein and TEA system was found to generate the most hydrogen. The parent complex was found to be the most active with TON of over 2100, and was also found to generate hydrogen from water obtained from a local lake, illustrating the robustness of the photochemical system.[5]

The efficacy of the iron polypyridyl complex family led to the consideration of incorporating the complex into heterogeneous systems by anchoring the complex onto TiO_2 NP to discover changes in photocatalytic activity. Some common anchoring groups for metal oxide semiconductor immobilization include silicanes, phosphonates, and carboxylates.[6] A 2004 study by Marcinko et al. found silicane anchoring groups on TiO_2 to hydrolyze in aqueous solutions, making it a poor candidate for use in water reduction systems. Marcinko et al. also examined phosphonate anchoring groups and found them to be highly stable on TiO_2 in aqueous environments.[7]

In 2011, Lakadamyali et al. designed an effective heterogeneous catalytic system by covalently bonding a cobaloxime catalyst and $Ru(bpy)_3^{2+}$ chromophore to TiO_2 with a phosphonate anchoring group. The system was found to only generate hydrogen when the catalyst and chromophore were anchored to TiO_2, illustrating the vital role of the covalently bound semiconductor for the success of the system.[8]

In 2018, our group utilized a phosphonate anchor group to immobilize **[$FeCl_2$(L)]** onto TiO_2 or $SrTiO_3$ to investigate the hydrogen generation from aqueous solutions with fluorescein chromophore and TEA electron donor.[9] The chromophore was not covalently bound to the TiO_2 with a phosphonic anchor as was done in the Lakadamyali system. This is due to the discovery that the fluorescein sensitized the TiO_2 surface without the need of an anchoring group modification, and the sensitization resulted in an increase of the absorbance in the visible spectrum (Figure 2.2). The TiO_2 supported catalyst was found to be more stable for longer, generating H_2 for 31 hours and resulting in 7800 TON. The $SrTiO_3$-immobilized catalyst ceased hydrogen generation after 10 hours of irradiation with an overall TON of 7000 after 31 hours. [9]

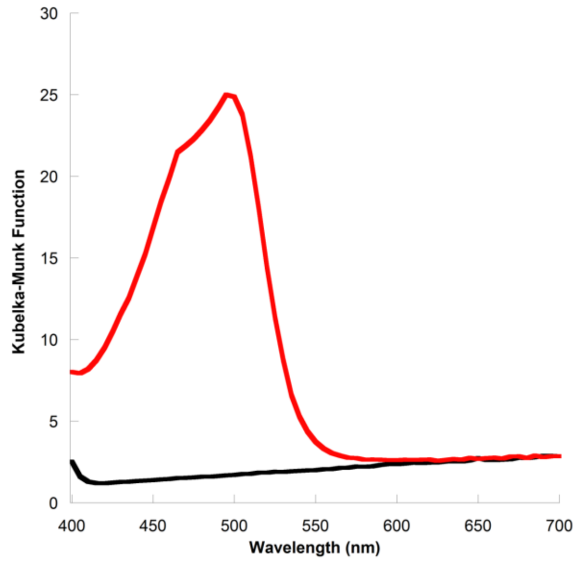

Figure 2.2. Diffuse Reflectance UV/Vis spectra of thin-film bare TiO_2 (black) and thin-film TiO_2 sensitized with fluorescein (red).[8]

While the TiO_2-phosphonate system was found to be highly effective at generating hydrogen with a nearly 4-fold improvement over the TON of **[$FeCl_2$(L)]**, the catalyst had to be synthesized by first immobilizing the ligand onto TiO_2, followed by complexing with iron (Figure 2.3). This was due to the strong binding of the phosphonic acid group, and attempts to complex the ligand with $FeCl_3$ resulted in the phosphonate preferentially binding with the iron center instead of the NNNO binding like the iron polypyridyl complex family. This resulted in an inability to characterize the complex with x-ray crystallography, as the complex could not be crystallized alone.

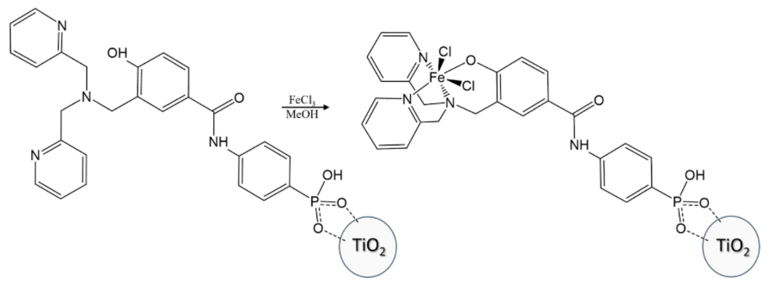

Figure 2.3. Phosphonic acid functionalized L on TiO_2 before and after complexing with $FeCl_3$ to form **[$FeCl_2$(L-PO_3)]**.

Carboxylic Acid Anchor

While carboxylic acids are considered to be more environmentally friendly than phosphonic acids, carboxylate anchoring groups have been stated to be weak and easily dissociated.[6] In 2013, Martini et al. investigated a variety of linkers with a Zn porphyrin complex on TiO_2 both with and without a Zn porphyrin complex using UV/vis. They reported that the phosphonate linker (Figure 2.4.L2), was stable in aqueous solutions before and after the addition of Zn porphyrin (Figure 2.4.L2a and L2b), which substantiates the phosphonic acid anchoring group stability found in our group.

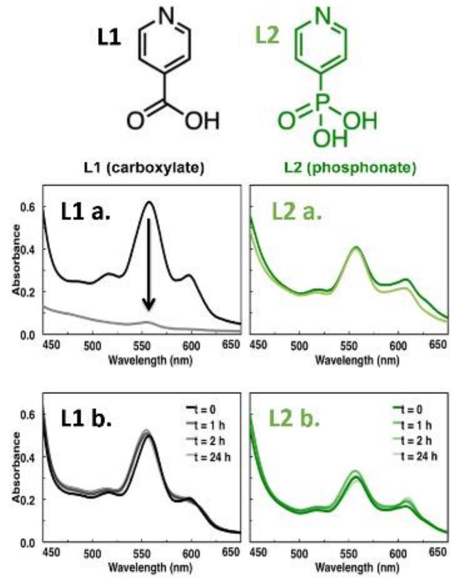

Figure 2.4. (L1) pyridine linker with carboxylate anchor; (L2) pyridine linker with phosphonate anchor; UV/Vis of linker on TiO_2 before (L1a and L2a) and after (L1b and L2b) Zn porphyrin complex.

When comparing the phosphonate and carboxylate linkers, the carboxylate linker alone was shown to be less stable. Even though Martini et al. found that the carboxylate linker was easily dissociated from the TiO_2 surface in aqueous solutions (Figure 2.4.L1 a), it was found that once the porphyrin complex was added to the linker, the carboxylate group did not dissociate and the complex and linker remained immobilized on the semiconductor surface (Figure 2.4.L1 b). Furthermore, the researchers found that the phosphonate linker provided worse electron injection than the carboxylate linker via terahertz spectroscopy probing the charge transfer from the porphyrin, through the linker, and into the CB of the TiO_2. They also used this method to determine the effect of the length of the linker as altered by the addition of a phenyl ring between the porphyrin and pyridine of the linker. They found a decrease in electron injection with increasing linker length, illustrating the benefit of short anchoring groups for electron transfer.[10] These results elucidate the benefits of a carboxylate anchor directly bound to the phenolate ring for immobilization of the catalyst onto TiO_2 and give promise to an improved method to incorporate the effective parent molecular catalyst into a heterogeneous system for water reduction.

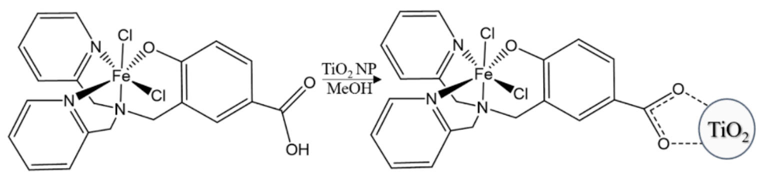

Figure 2.5. Carboxylic acid functionalized iron polypyridyl complex before and after immobilizing on TiO_2 to form **[FeCl$_2$(L-COOH)]**.

In this chapter, synthesis, characterization, and electro- and photochemical analysis are presented for an iron polypyridyl complex functionalized with a carboxylate anchor, **[FeCl$_2$(L-COOH)]**, for immobilization on TiO_2 NP. The ligand was characterized using nuclear magnetic resonance (NMR) and mass spectrometry (MS), and the catalyst was able to be complexed prior to the immobilization of the ligand onto TiO_2. The complex was characterized using single crystal x-ray crystallography and was investigated electrochemically for catalytic activity. Immobilization of the catalyst onto TiO_2 was done via thin-film and centrifuge methods and confirmed using diffuse reflectance UV/Visible spectroscopy (UV/vis). The heterogeneous catalyst was assessed photochemically for its ability to generate hydrogen in aqueous solutions. The goal of this project was to design a more effective photocatalyst that could be characterized prior to immobilization onto TiO_2.

Methods

Materials

P25 TiO_2 was obtained from Acros Organics. The TiO_2 nanoparticles are 25 nm in diameter on average and are 70% anatase and 30% rutile. Zirconia (diameter = 20 nm) was purchased from Sigma Aldrich. 4-hydroxybenzoic acid, hexamethylenetetramine, trifluoroacetic acid, sodium cyanoborohydride were all obtained from Acros Organics. Bis(pyridin-2-ylmethyl)amine was obtained from TCI.

Synthesis

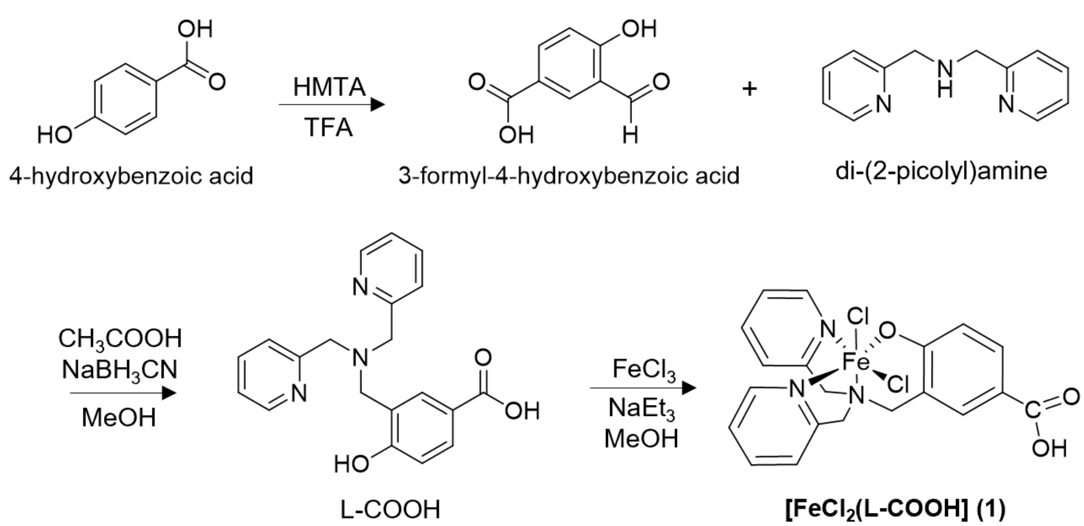

Figure 2.6. Synthesis of **[$FeCl_2$(L-COOH)].**

Synthesis of L-COOH (Figure 2.6)

L-COOH was synthesized according to a modified literature procedure.[1,10] 4-hydroxybenzoic acid (2.5 g, 18 mmol) was added to a round bottom flask with a stir bar and dissolved in trifluoroacetic acid (TFA). Hexamethylenetetramine (HMTA, 2.5 g, 18 mmol) was then added to the flask dropwise, then capped with a condenser and allowed to reflux for 24 hours. Hydrochloric acid was then added to the solution and stirred for 6 hours. The solid product, 3-formyl-4-hydroxybenzoic acid, was collected by filtration. 3-formyl-4-hydroxybenzoic acid (1 g, 6 mmol) was then added to a flask and dissolved in methanol and acidified with 3 drops of acetic acid. Di-(2-picolyl)amine (1.04 mL, 6 mmol), followed by a methanolic solution of cyanoborohydride (0.182 g, 3 mmol), was added to the flask dropwise, topped with a condenser, and allowed to reflux 24 hours. The solution was then adjusted to pH 4 with HCl and evaporated until dry. The solution was then dissolved in 50 mL of saturated $NaHCO_3$ solution and extracted with DCM (3 x 50 mL). 1 M HCl was added to the aqueous layer until it reached pH 7. The aqueous layer was extracted again with DCM (3 x 50 mL). The organic layers were combined and dried with $MgSO_4$, filtered, and evaporated to collect L-COOH**.** The ligand synthesis was confirmed with NMR (Figure A3 and A4) and high resolution mass spectrometry (Figure A5).

Synthesis of **[$FeCl_2$(L-COOH)]**

[$FeCl_2$(L-COOH)] was synthesized using a modified procedure.[1] A methanolic solution of L-COOH was added to a vial with a methanolic solution of $FeCl_3$•$6H_2O$ and sodium methoxide and allowed to stir at room temperature for 1 hour. The solution was filtered through celite, and the purple solid was collected, dissolved in minimal DCM, and crystals were obtained by slow diffusion into diethyl ether.

TiO_2 Film Preparation

TiO_2 NP and deionized water were added to a vial in a 4.0 g : 7.0 mL ratio. The mixture was stirred for approximately four hours to form a slurry. After stirring, the mixture was transferred onto one side of a microscope slide taped off with scotch tape via a Pasteur pipette. The slide was doctor bladed by scraping the TiO_2 slurry across the slide using a razor blade to result in a thin, even layer.[10] The doctor bladed thin films were heated in a muffle furnace at 300°C for two hours.

Catalyst Immobilization on TiO_2

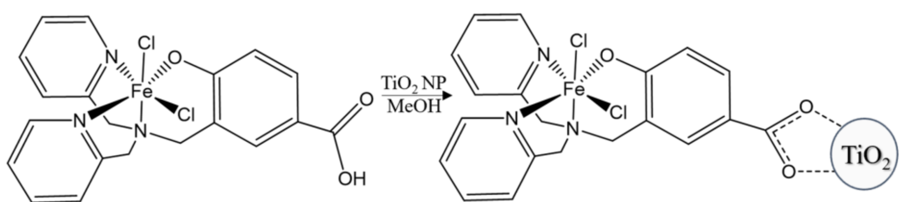

Figure 2.7. Carboxylic acid functionalized complex before (**1**) and after (**2**) immobilization onto TiO_2.

The catalyst was immobilized on the semiconductor surface by soaking the nanoparticles in a methanolic solution of **1**, followed by centrifugation. Excess catalyst solution (8×10^{-8} mol catalyst in methanol per 5 mg of semiconductor) was added to a sample vial, along with a measured amount (20-100 mg) of semiconductor nanoparticles. Excess methanol was added to the sample vial, bringing the total volume to 5.0 mL. The sample vial was stirred for one hour and divided into microcentrifuge tubes to be centrifuged at 13,400 rpm for 15 minutes. The supernatant was removed, followed by the addition of methanol to the microcentrifuge tubes to rinse the nanoparticles. The mixtures were shaken and sonicated before being centrifuged for three minutes. This wash process was completed a total of four times. Following the final centrifugation, the supernatant was removed and the catalyst-sensitized nanoparticles were allowed to dry in dark conditions for 12 hours.

Electrochemical Studies

Cyclic Voltammetry

All electrochemical experiments were performed under an argon atmosphere using CH Instruments 620D potentiostat and CH Instruments 680 amp booster. Cyclic voltammograms (CV) were taken using a standard three-electrode cell, including a saturated calomel electrode (SCE), platinum auxiliary electrode, and glassy carbon working electrode. The platinum and glassy carbon electrodes were polished prior to each CV using 0.05 μm alumina powder on a cloth-covered polishing pad and rinsed thoroughly with deionized water and acetonitrile.

Acid Addition Study

5.0 mL acetonitrile, 0.2 g tetrabutylammonium hexafluorophosphate ($TBAPF_6$, 0.1M), and roughly 0.3 mg of **[$FeCl_2$(L-COOH)]** (0.1 mM) were added to an electrochemical cell and degassed with argon for 15 minutes. CVs were taken without acid, and after the addition of 20, 40, 60, 80, and 100 uL of 0.11 M TFA. The CV was taken at a potential range from -0.4 to -1.8 V vs Fc^+/Fc with a scan rate of 0.2 V/s.

Catalyst Addition Study

5.0 mL acetonitrile, 0.2 g $TBAPF_6$, (0.1M), and 100 μL 1.1 M TFA were added to an electrochemical cell and degassed with argon for 15 minutes. CVs were taken without catalyst, and after the addition of 112, 224, 336, and 448 μL of **[$FeCl_2$(L-COOH)]**. The CV was taken at a potential range from -0.4 to -1.8 V vs Fc^+/Fc with a scan rate of 0.2 V/s.

Photochemical Studies

Hydrogen Evolution Studies

Hydrogen evolution was determined using test tubes with 1:1 ethanol: deionized water solvent, varying amounts of **[$FeCl_2$(L-COOH)]**, 1.8 mM fluorescein, and 5% triethylamine (TEA, v/v%). Immediately after the addition of TEA, test tubes were sealed with a septa and copper wire and degassed with argon for 10 minutes. A Hamilton syringe was used to remove 1.0 mL argon from the headspace of the test tube and then 1.0 mL of methane was added as an internal standard. The test tubes were irradiated with LED lights while stirring. After irradiation, 0.10 mL of headspace was removed using a Hamilton gas syringe and injected into a gas chromatograph to determine the ratio of hydrogen to methane to determine hydrogen produced.

System Optimization Studies

The general procedure for hydrogen evolution studies was followed while varying catalyst concentration, chromophore concentration, or wavelength of LED light. Comparison of TONs were made between 0.5 mg, 1 mg, and 5 mg of catalyst-functionalized nanoparticles; green 560 nm versus blue 490 nm LED light; and 1.8, 1.9, 2.0, 2.1, 2.2, 2.3, and 2.4 mM fluorescein in EtOH solutions at specific time points to determine the optimal setup for the system, which were carried out in further hydrogen evolution studies. The highest TONs were achieved using 0.5 mg of catalyst-functionalized nanoparticles and 2.1 mM fluorescein in the blue LED light setup.

Reusability Studies

Samples were prepared following the same procedure as in the hydrogen evolution studies with 5 mg of catalyst-functionalized nanoparticles rather than 0.5 mg. Following 25 hours of irradiation, samples were removed from the blue LED setup, filtered to remove **2**, and filtrate was centrifuged at 5,000 rpm for 12 minutes. Following centrifugation, the supernatant was removed and the recycled nanoparticles were rinsed with ethanol. Along with the nanoparticles, fresh fluorescein, triethylamine, water, and ethanol were added to sample test tubes that were then capped with septa and sealed with copper wire. After degassing for ten minutes with argon, a Hamilton gas syringe was used to remove 1.0 mL of headspace from each test tube and add 1.0 mL methane gas as an internal standard. Test tubes were placed back in the blue LED light setup for irradiation while stirring. A Hamilton gas syringe was used to remove 0.10 mL of headspace gas from each test tube and injected into a gas chromatograph for analysis at various time intervals.

Results and Discussion

A main benefit of using the carboxylate anchoring group is the ability to characterize the complex before immobilizing onto TiO_2. Crystals of the complex were obtained using slow diffusion of diethyl ether into a highly concentrated solution of **1** in DCM. A structure of the catalyst was obtained via x-ray crystallography and was found to be a distorted octahedral geometry (Figure

2.8). The Fe-N bonds are between 2.17 and 2.24 Å in length, but the Fe-O bond is shorter at 1.91 Å. Distortions from the typical 180° axial or 90° equatorial spacings include the O(1)-Fe(1)-N(2), N(1)-Fe(1)-Cl(1), and N(3)-Fe(1)-Cl(2) axial bond angles of 162-170° and the N(2)-Fe(1)-N(1) and N(3)-Fe(1)-N(1) equatorial bonds exhibiting 73.5-76.3° bond angles(Table 2.1). These distortions are consistent with other complexes in the iron polypyridyl family.[1–3] The carboxylic acid functional groups allow for the formation of a dimer via hydrogen bonding between a pair of molecules (Figure 2.9).

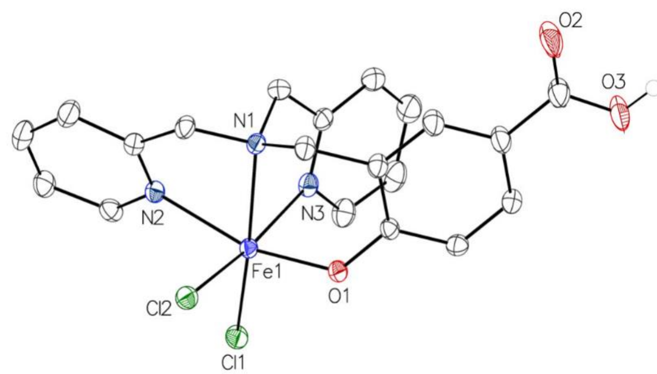

Figure 2.8. ORTEP diagram of **1**. Fe (dark blue), O (red), Cl (green), N (blue), C (white). Ellipsoids are at the 50% probability level and all hydrogen atoms besides carboxylic hydrogen have been omitted for visual clarity.

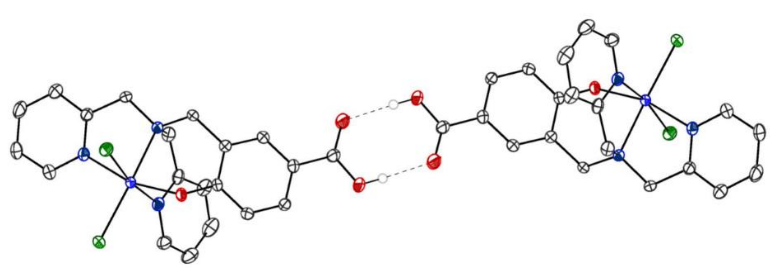

Figure 2.9. Diagram of dimer formed by hydrogen bonding of carboxylic groups of **1.**

Table 2.1. Bond lengths and angles of Fe for **[$FeCl_2$(L-COOH)]**

Bond	Bond Lengths (Å)
Fe(1)-Cl(1)	2.2922(5)
Fe(1)-Cl(2)	2.3194(5)
Fe(1)-O(1)	1.9119(13)
Fe(1)-N(1)	2.2410(16)
Fe(1)-N(2)	2.1716(16)
Fe(1)-N(3)	2.2063(16)
Bonds	**Bond angles (°)**
Cl(1)-Fe(1)-Cl(2)	98.15(2)
O(1)-Fe(1)-Cl(1)	99.59(4)
O(1)-Fe(1)-Cl(2)	94.93(5)
O(1)-Fe(1)-N(1)	89.05(6)
O(1)-Fe(1)-N(2)	162.51(6)
O(1)-Fe(1)-N(3)	84.45(6)
N(1)-Fe(1)-Cl(1)	164.51(5)
N(1)-Fe(1)-Cl(2)	93.84(4)
N(2)-Fe(1)-Cl(1)	97.08(5)
N(2)-Fe(1)-Cl(2)	87.85(5)
N(2)-Fe(1)-N(1)	73.52(6)
N(2)-Fe(1)-N(3)	89.88(6)
N(3)-Fe(1)-Cl(1)	91.63(5)
N(3)-Fe(1)-Cl(2)	170.16(5)
N(3)-Fe(1)-N(1)	76.34(6)

Electrochemical characterization is also possible with the formation of the complex before immobilization on TiO_2. One notable characteristic of all complexes in this iron polypyridyl family is the anodic shift of the reversible reduction of Fe(III) to Fe(II). Without the addition of a proton source, the iron reduction occurs at roughly -0.6 V vs Fc^+/Fc. Once a proton source, trifluoroacetic acid (TFA) is added, the redox peak shifts and the iron reduction occurs near -0.4 V vs Fc^+/Fc (Figure 2.10). This alludes to this carboxylate functionalized catalyst having a similar HER mechanism to that of the parent complex, with the protonation of the phenolate moiety occurring first in the presence of acid.[1] This corresponds to a CECE or CEEC mechanism, where C represents protonation and E represents reduction.

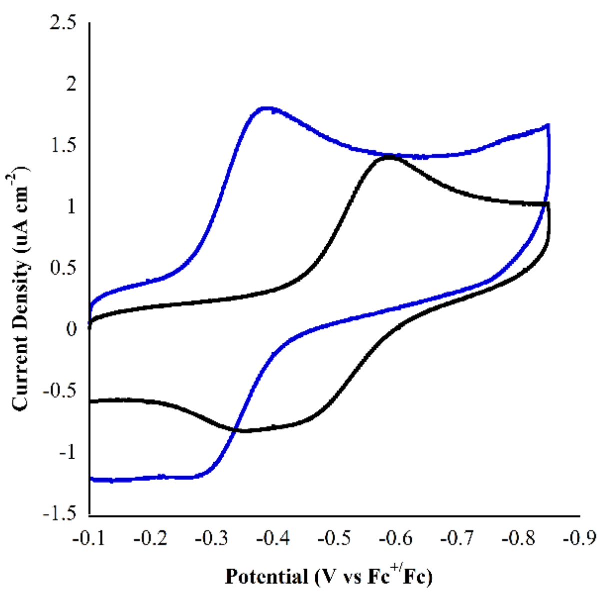

Figure 2.10. Redox peaks of **1** before (black) and after (blue) the addition of TFA.

To assess **1** for the ability to reduce protons, CVs from -0.4 to -1.7 V vs. Fc^+/Fc were taken without acid and with increasing aliquots of 0.11 M TFA. An irreversible catalytic wave occurs at -1.55 V vs. Fc^+/Fc and increases linearly with each 20uL addition, indicating a second-order dependance on protons. This results in an i_c/i_p of 8.7 with the final TFA concentration of 2.2 mM (Figure 2.11). **1** operates at an overpotential of 790 mV in the presence of 1 mM TFA.

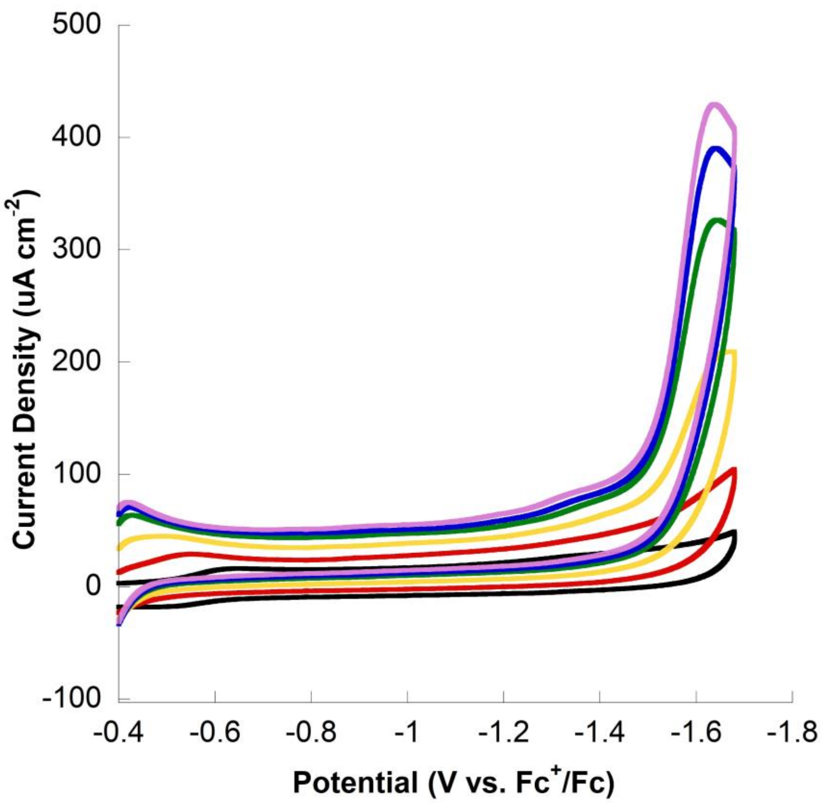

Figure 2.11. CVs of **1** with no acid (black), 0.44 (red), 0.88 (yellow), 1.32 (green), 1.76 (red), and 2.2 mM (purple) TFA.

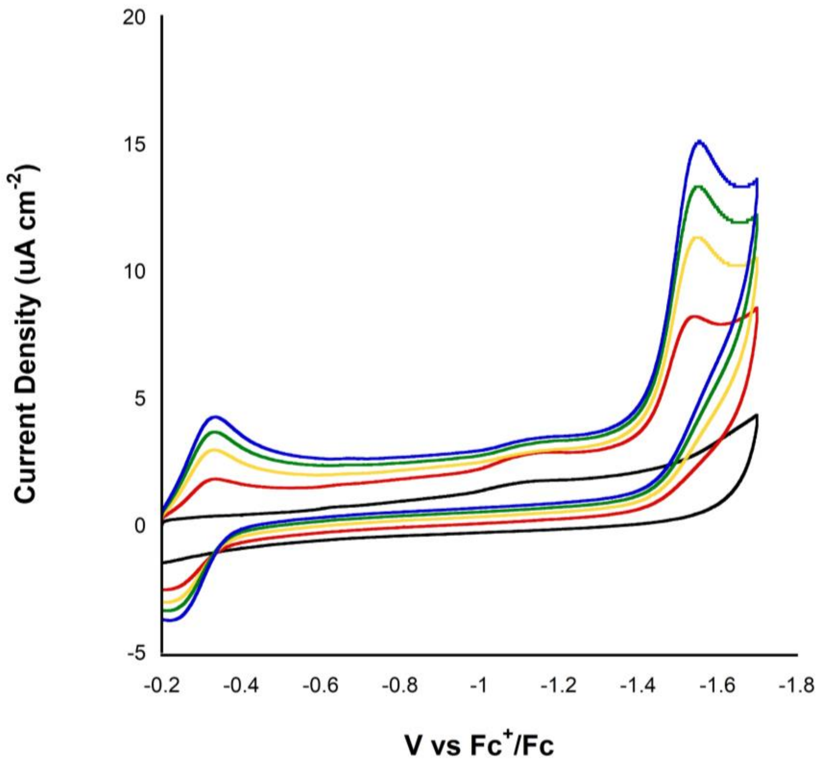

Figure 2.12. CVs of 2.2 M TFA only (black) and 0.1 (red), 0.2 (yellow), 0.3 (green), and 0.4 mM (blue) **1.**

CVs of increasing concentrations of **1** with steady TFA concentrations show a linear increase with each addition of catalyst (Figure 2.12). This is also the case for the parent catalyst, indicating that there is a first-order dependance on **1**, giving a rate expression of rate=k[**1**][H+]^2.

When compared to the parent complex with an i_c/i_p of 7.8 and irreversible reduction at -1.57 V, **1** has a higher i_c/i_p and has a lower overpotential, indicating that the carboxylate anchor did not hamper the electrocatalytic ability to reduce protons or change the reaction mechanism or rate expression, but rather was slightly more active and efficient than the parent complex.

Immobilization of **1** on TiO_2 surface to form **2** was confirmed by diffuse-reflectance UV/vis spectra, with a strong increase in absorbance in the visible spectrum and a peak around 590 nm (Figure 2.13). An absorbance in this region is consistent with others in the iron polypyridyl family and is indicative of pπ–dπ* transition from the phenolate to the iron center.[8]

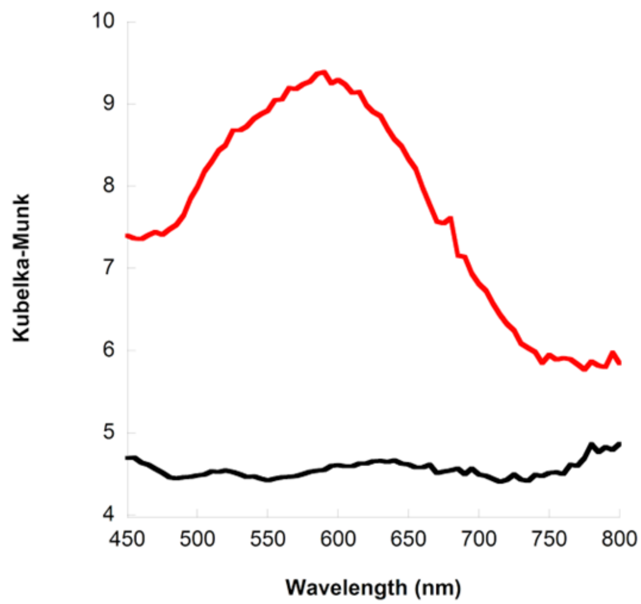

Figure 2.13. UV/Vis spectra of blank TiO_2 (black) and **2** (red).

When incorporating the catalyst into a photocatalytic system, fluorescein was chosen as the chromophore due to its ability to reduce similarly negative proton reduction potentials and success in photochemical studies of the iron polypyridyl family. System optimization included variations in Fl and catalysts concentrations, and optimum conditions were found to be 2.1 mM Fl and 0.5 mg **2**. LED light wavelengths used to irradiate the photochemical system were also investigated. The molecular catalysts were found to perform best under 560 nm green light, but immobilization on TiO_2 allowed for higher TONs with 490 nm blue LEDs. Studies of **1** in a homogenous photochemical system irradiated by blue light produced TONs of 160 over 24 hours, a nearly 75-fold reduction in activity. The 490 nm wavelength corresponds more closely to the 495 nm Fl absorbance, but Fl cannot quench quickly enough and photo-bleaches in the homogeneous system due to diffusion-based kinetics, ceasing hydrogen generation before higher TONs can be achieved. This illustrates the benefit of catalyst immobilization and Fl aggregation on TiO_2 NPs for the stability and increased efficiency of the heterogeneous photocatalytic system. Due to these findings, all TONs reported in this chapter were obtained with blue LEDs.

Time course studies over 48 hours demonstrate TOFs of 1,000 hr^{-1} for the first 10 hours, with subsequent hydrogen generation slowing and ceasing by 48 hours with a system of 0.5 mg **2**, 2,1 mM Fl, and 5% TEA in 1:1 H_2O:EtOH. TONs reached over 12,000 over the 48 hours period (Figure 2.14).

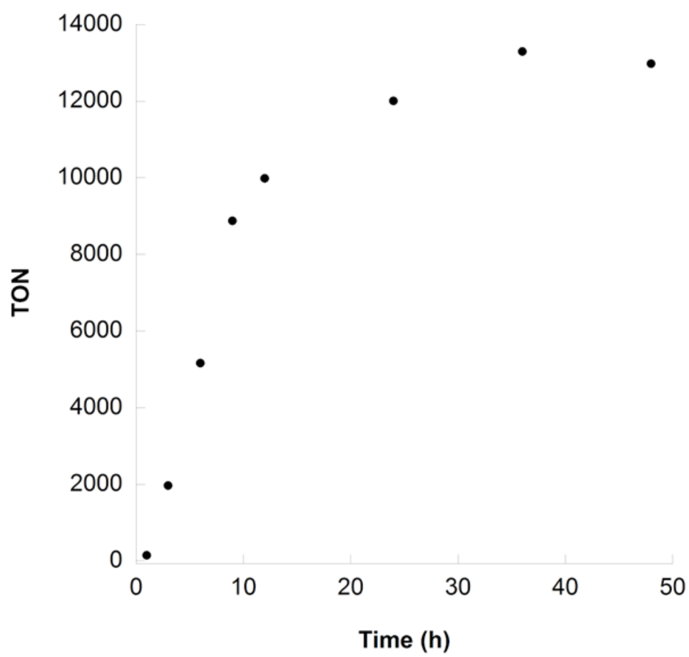

Figure 2.14. TONs over 48 hours in 2.1mM Fl, 5% TEA, and 0.5mg **2** 1:1 H_2O:EtOH photochemical system.

To test the robustness and reusability of the **2**, 5 mg **2** was used in the photocatalytic system and irradiated for 25 hours. NPs were then filtered from the solution and cleaned and centrifuged and reused with fresh Fl, TEA, and water-ethanol solution. Hydrogen generation resumed for over 10 hours and generated similar TONs that were seen with fresh NPs. These results demonstrate the robustness of the TiO_2 immobilization, confirming the ability of the carboxylate functional group to effectively anchor **1** to the TiO_2 NPs.

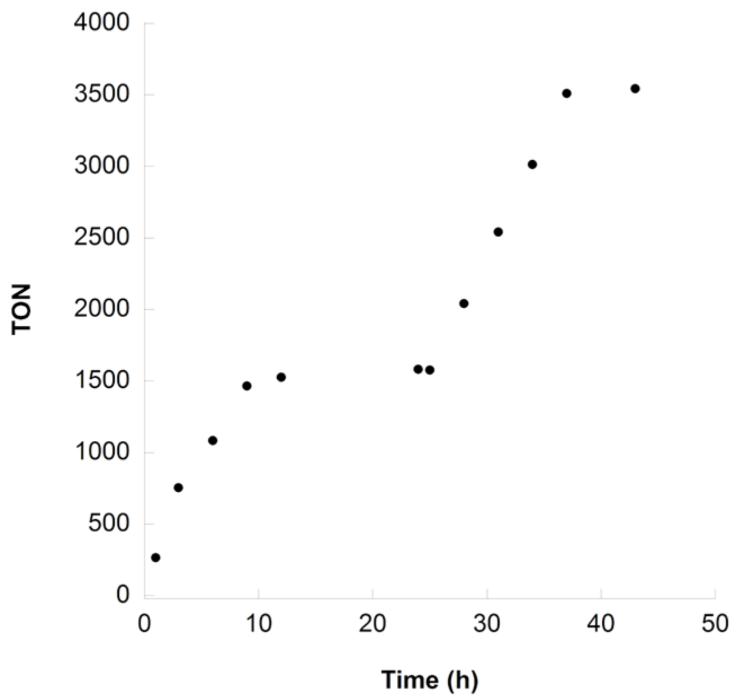

Figure 2.15. TONs over 48 hours in 2.1 mM Fl, 5% TEA, and 5 mg **2** in 1:1 H_2O:EtOH photochemical system. NP were recycled at 25 hours and reused in fresh Fl and TEA.

Hydrogen Generation from Seawater

While hydrogen generation from deionized water exemplifies the catalytic ability of **2** in a pure system, water requires rigorous processing to be deionized and may not be readily available. To elucidate the robustness of the catalyst and probe the ability of **2** to generate hydrogen in other conditions, water from Virginia Beach, VA, was collected, filtered, and used in place of DI water under photocatalytic conditions. The sea water system generated 93 µL hydrogen over 24 hours, which is a 58% decrease from the 221 µL H_2 generated using DI water. While this showed that sea water allowed for less than half of the amount of hydrogen than DI water under the same conditions and concentrations of **2**, it is a vitally important proof of concept that **2** is robust enough to generate hydrogen in impure systems.

Conclusion

These studies explicate the benefit of the carboxylic acid functional group due to its ability to be complexed and characterized, as well as show highly effective photocatalytic ability when immobilized on TiO_2 NP. The use of carboxylic acid instead of phosphonic acid as an anchoring group allows for the design of a more environmentally-friendly catalyst that can be complexed with iron and crystalized to obtain a crystal structure. The distorted octahedral geometry parallels that of the other complexes in the iron polypyridyl family, and electrochemical activity of **1** demonstrates modest improvements in activity with increased i_c/i_p, similar overpotentials, and a similar proton reduction mechanism to the parent complex. Successful immobilization on TiO_2 allows for the incorporation of **1** into a highly efficient and recyclable heterogeneous photocatalytic system to form **2**, generating TONs over 12,000 and is able to be recycled for continuous hydrogen generation. The immobilized NP are stable enough to generate hydrogen from seawater, alluding to potential real world uses for use as a heterogeneous catalyst for clean energy and water applications.

References

1. Du, P.; Eisenberg, R. Catalysts Made of Earth-Abundant Elements (Co, Ni, Fe) for Water Splitting: Recent Progress and Future Challenges. *Energy Environ. Sci.* **2012**, *5* (3), 6012–6021. https://doi.org/10.1039/C2EE03250C
2. Connor, G. P.; Mayer, K. J.; Tribble, C. S.; McNamara, W. R. Hydrogen Evolution Catalyzed by an Iron Polypyridyl Complex in Aqueous Solutions. *Inorg. Chem.* **2014**, *53* (11), 5408–5410. https://doi.org/10.1021/ic500069c.
3. Cavell, A. C.; Hartley, C. L.; Liu, D.; Tribble, C. S.; McNamara, W. R. Sulfinato Iron(III) Complex for Electrocatalytic Proton Reduction. *Inorg. Chem.* **2015**, *54* (7), 3325–3330. https://doi.org/10.1021/ic5030394.
4. Hartley, C. L.; DiRisio, R. J.; Chang, T. Y.; Zhang, W.; McNamara, W. R. Electrocatalytic Hydrogen Evolution by an Iron Complex Containing a Nitro-Functionalized Polypyridyl Ligand. *Polyhedron* **2016**, *114*, 133–137. https://doi.org/10.1016/j.poly.2015.11.023.
5. Hartley, C. L.; DiRisio, R. J.; Screen, M. E.; Mayer, K. J.; McNamara, W. R. Iron Polypyridyl Complexes for Photocatalytic Hydrogen Generation. *Inorg. Chem.* **2016**, *55* (17), 8865–8870. https://doi.org/10.1021/acs.inorgchem.6b01413.
6. Geldof, D.; Tassi, M.; Carleer, R.; Adriaensens, P.; Roevens, A.; Meynen, V.; Blockhuys, F. Binding Modes of Phosphonic Acid Derivatives Adsorbed on TiO2 Surfaces: Assignments of Experimental IR and NMR Spectra Based on DFT/PBC Calculations. *Surf. Sci.* **2017**, *655*, 31–38. https://doi.org/10.1016/j.susc.2016.09.001.
7. *Hydrolytic Stability of Organic Monolayers Supported on TiO2 and ZrO2* | *Langmuir*. https://pubs.acs.org/doi/10.1021/la034914l (accessed 2023-04-06).
8. Lakadamyali, F.; Reisner, E. Photocatalytic H2 Evolution from Neutral Water with a Molecular Cobalt Catalyst on a Dye-Sensitised TiO2 Nanoparticle. *Chem. Commun.* **2011**, *47* (6), 1695–1697. https://doi.org/10.1039/C0CC04658B.
9. Race, N. A.; Zhang, W.; Screen, M. E.; Barden, B. A.; McNamara, W. R. Iron Polypyridyl Catalysts Assembled on Metal Oxide Semiconductors for Photocatalytic Hydrogen Generation. *Chem. Commun.* **2018**, *54* (26), 3290–3293. https://doi.org/10.1039/C8CC00453F.
10. Martini, L. A.; Moore, G. F.; Milot, R. L.; Cai, L. Z.; Sheehan, S. W.; Schmuttenmaer, C. A.; Brudvig, G. W.; Crabtree, R. H. Modular Assembly of High-Potential Zinc Porphyrin Photosensitizers Attached to TiO2 with a Series of Anchoring Groups. *J. Phys. Chem. C* **2013**, *117* (28), 14526–14533. https://doi.org/10.1021/jp4053456.
11. Talukdar, D.; Panda, S.; Borah, R.; Manna, D. Membrane Interaction and Protein Kinase C-C1 Domain Binding Properties of 4-Hydroxy-3-(Hydroxymethyl) Phenyl Ester Analogues. *J. Phys. Chem. B* **2014**, *118* (27), 7541–7553. https://doi.org/10.1021/jp5044305.
12. *Acetylacetonate Anchors for Robust Functionalization of TiO2 Nanoparticles with Mn(II)−Terpyridine Complexes* | *Journal of the American Chemical Society*. https://pubs.acs.org/doi/10.1021/ja805498w (accessed 2023-04-06).

13. Wise, C. F.; Liu, D.; Mayer, K. J.; Crossland, P. M.; Hartley, C. L.; McNamara, W. R. A Nickel Complex of a Conjugated Bis-Dithiocarbazate Schiff Base for the Photocatalytic Production of Hydrogen. *Dalton Trans.* **2015**, *44* (32), 14265–14271. https://doi.org/10.1039/C5DT02042E.

Appendix A

Surface Coverage Determination

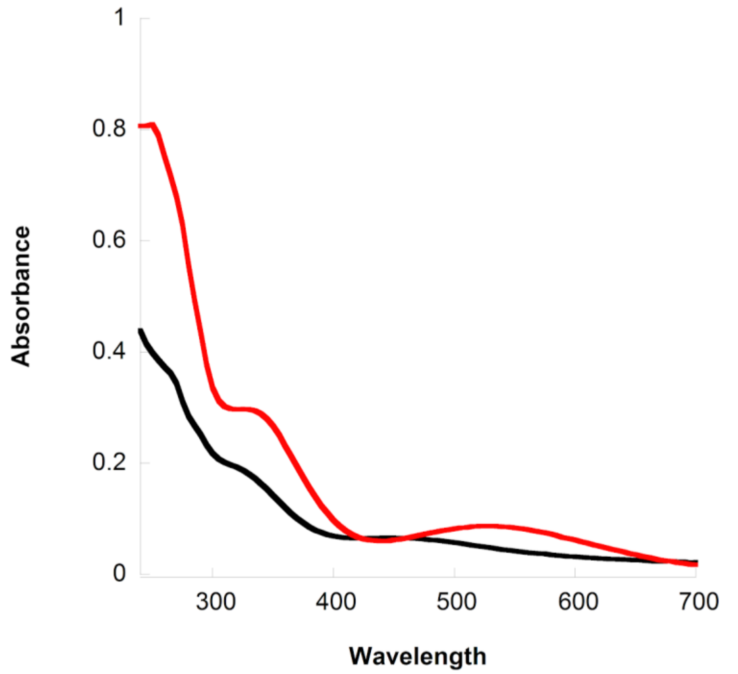

Figure A1. UV-Vis absorption spectra of dilute **2** solution (red) and supernatant (black).

UV-Vis spectrophotometry was used to determine the ligand coverage on TiO_2 as outlined in previously reported procedures.[12, 13] A 4.0 x 10^{-5} M solution of complex in methanol was prepared and analyzed via UV-Vis. 4.0 mL sample of **1** in a MeOH solution was then added to a sample vial with 5.0 mg of TiO_2 nanoparticles, capped, and stirred for one hour. The mixture was divided into microcentrifuge tubes and centrifuged at 13,400 rpm for 15 minutes. After centrifugation, the supernatant was collected and also analyzed via UV-Vis. The absorbance of the supernatant and original complex solution were compared at ~260 nm, and the difference in absorbance between the solution and supernatant was used to calculate the number of moles of ligand immobilized on the semiconductor surface. A sample calculation is shown below:

$$mol\ \mathbf{1} = \left[1 - \left(\frac{supernatant\ absorbance}{original\ complex\ solution\ absorbance}\right)\right] \times (4.0 \times 10^{-5}\ M)$$

$$\times (4 \times 10^{-3}\ L)$$

$$= \left[1 - \left(\frac{0.40}{0.81}\right)\right] \times (4.0 \times 10^{-5}\ M) \times (4 \times 10^{-3}\ L)$$

$$= \ 8.00\ \times 10^{-8}\ moles\ per\ 5\ mg\ nanoparticles$$

Calculation of Turnover Number

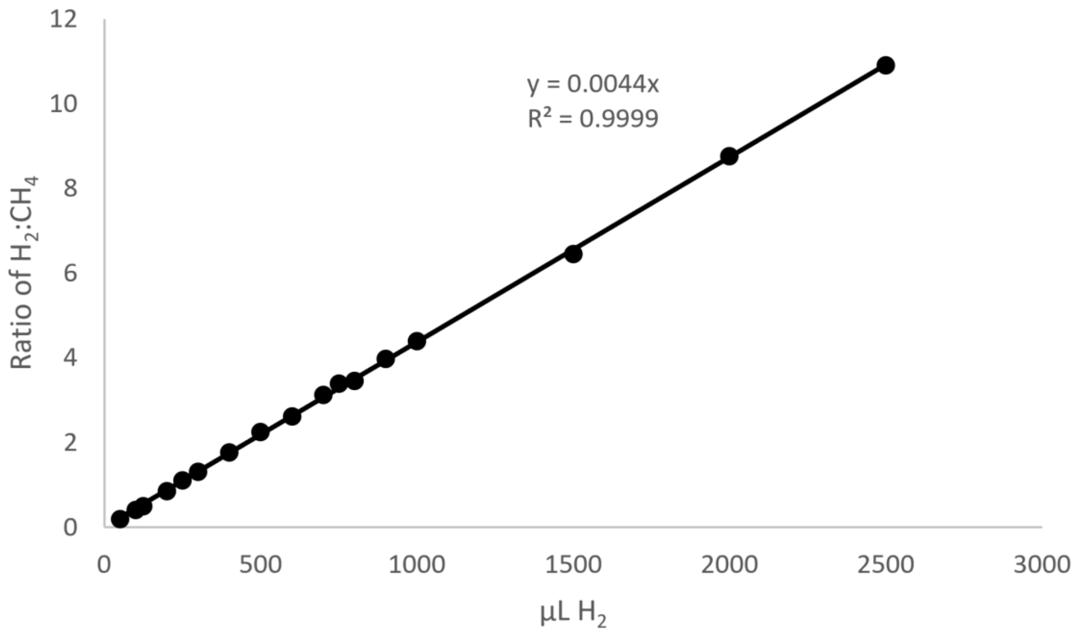

Figure A2. Calibration curve of H_2 to CH_4 peak areas used for determination of hydrogen generation. The ratio of peak areas was plotted against the volume of H_2 injected into the GC.

Turnover number (TON) is defined as the moles of product generated per mole of catalyst. To determine the TON for hydrogen generated by our catalyst, a calibration curve has been developed by injecting a known amount of hydrogen, as well as the internal standard, methane, into the gas chromatograph (GC). The ratio of the obtained hydrogen and methane peaks are then plotted versus the volume of injected hydrogen. The calibration curve used for this study resulted in a slope of 0.0044 and is used to determine the volume, and therefore moles, of hydrogen generated from the system.[9,13] The equation is as follows:

$$\mu L\ H_2 = \frac{1}{0.0044}\left(\frac{Area\ H_2}{Area\ CH_4}\right)$$

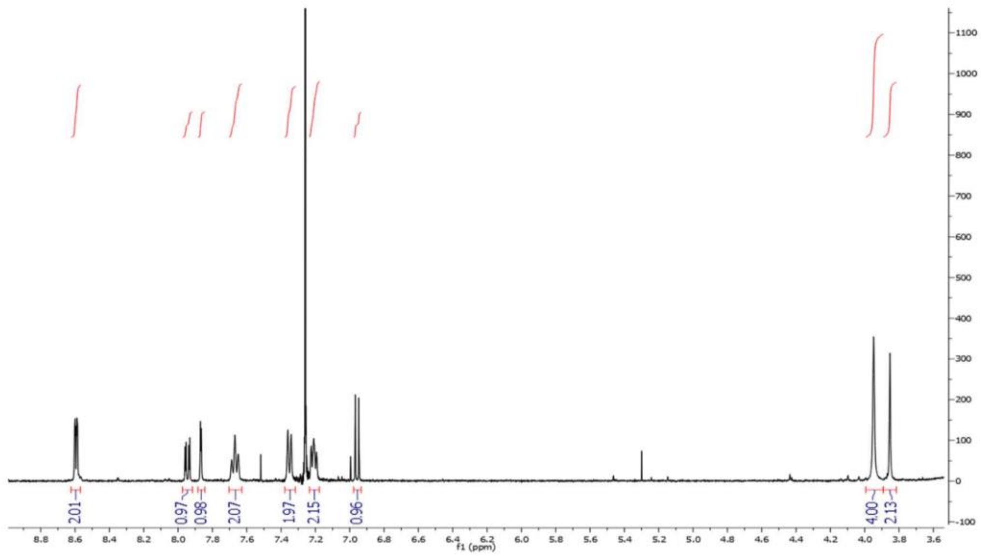

Figure A3. ^{1}H NMR spectrum of L-COOH with integrations in blue.

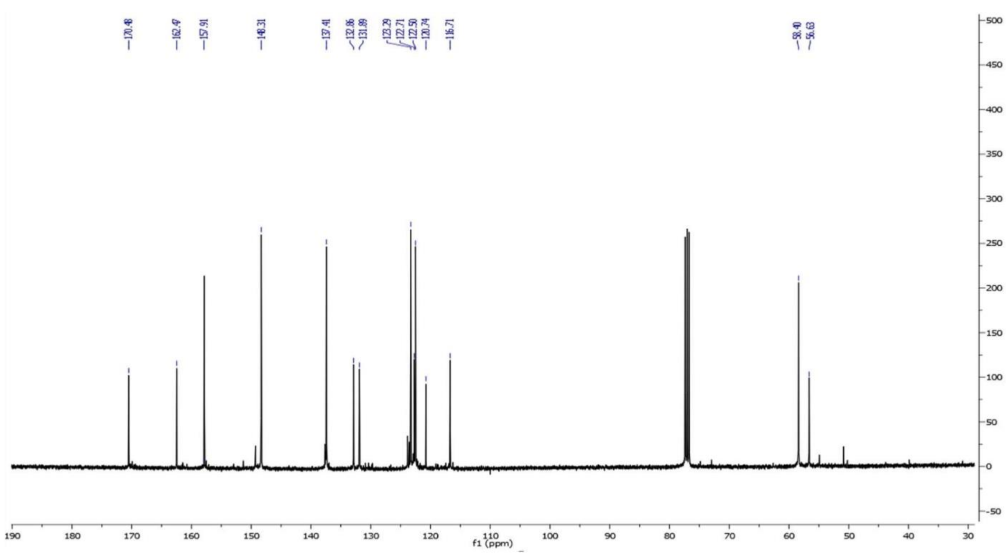

Figure A4. ^{13}C NMR spectrum of L-COOH.

Sample Name: WRM013
Exact Mass of $C_{20}H_{19}N_3O_3Na^+$ = 372.131863 u
Observed Mass = 372.131849 u
Difference = < 1.0 ppm

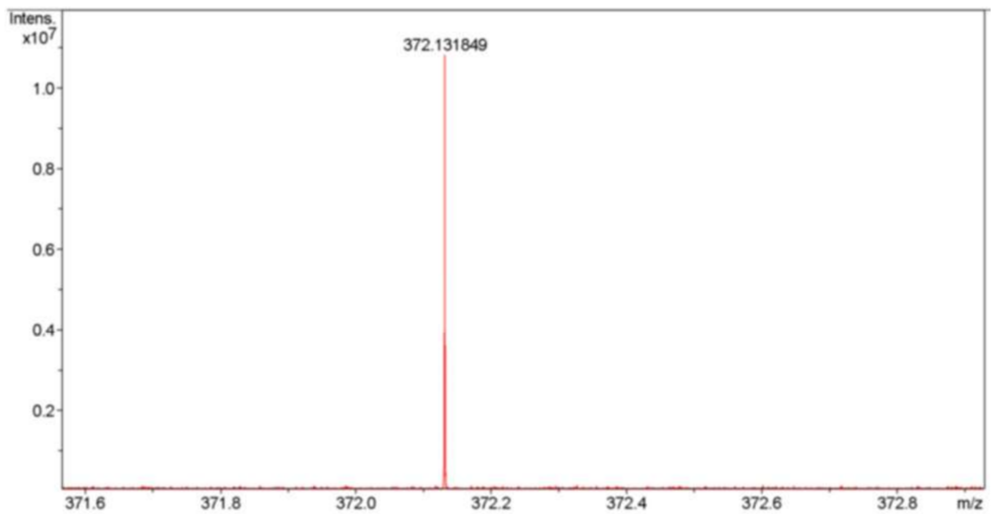

Figure A5. High resolution mass spectrum of L-COOH. The expected molecular ions were observed with a difference of less than 1 ppm.

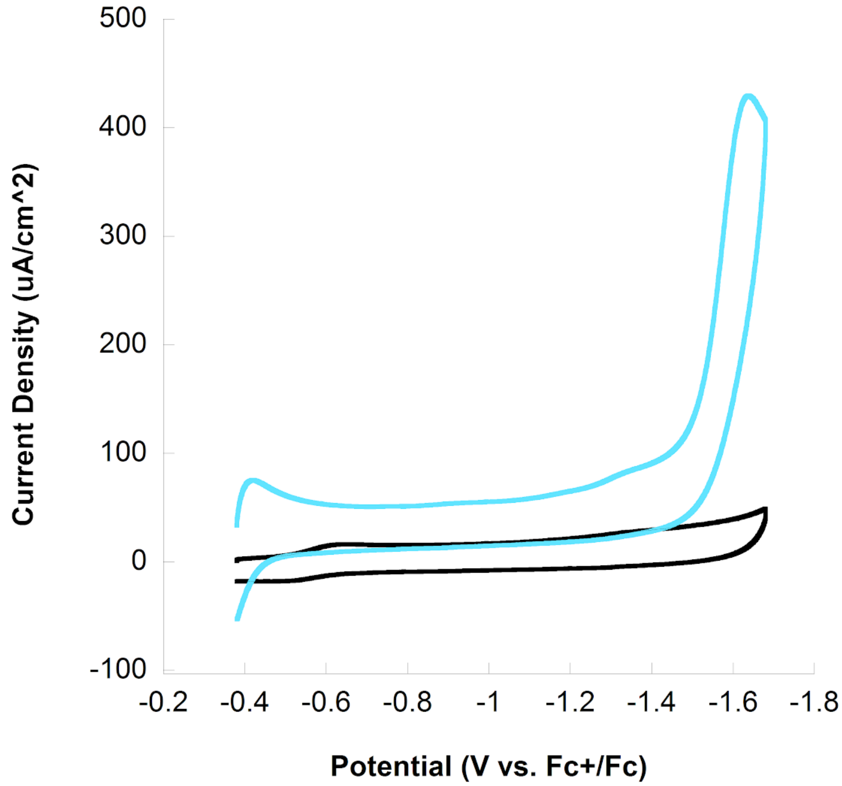

Figure A6. CV of **1** with (blue) and without (black) 100 µL of 0.11 M TFA.

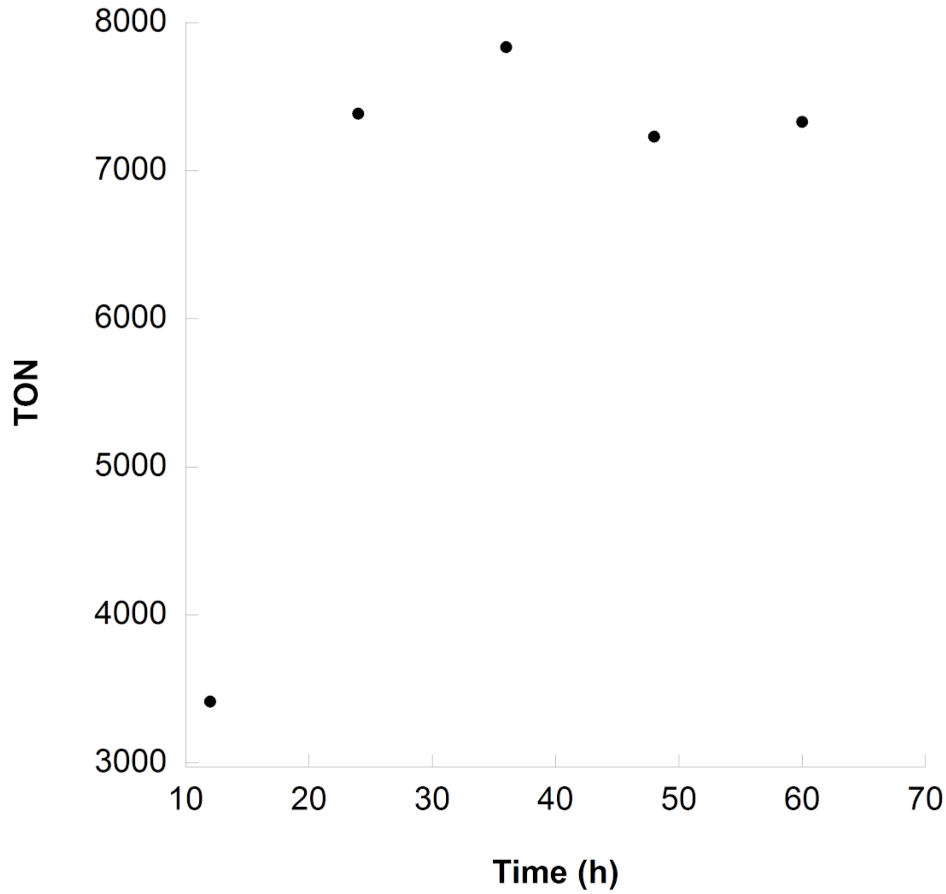

Figure A7. Hydrogen evolution over 60 hours using 1 mg of **2**, 2.1 mM Fl, 5% TEA in 1:1 H_2O:EtOH, irradiated with green LED light.

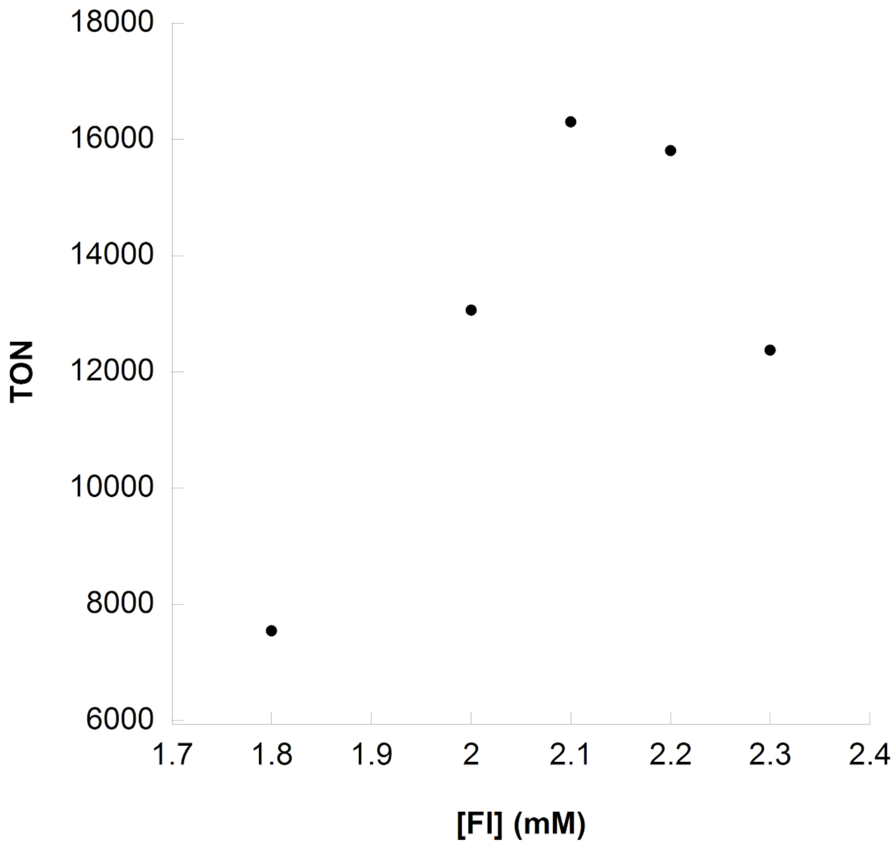

Figure A8. TON vs. [Fl] (mM) with 0.5 mg of **2** and 5% TEA in 1:1 H_2O:EtOH after 12 hours.

Table A1. Crystal data and structure refinement for **1**

Identification code	cwmwm13	
Empirical formula	C20 H18 Cl2 Fe N3 O3	
Formula weight	475.12	
Temperature	100.00(10) K	
Wavelength	1.54184 Å	
Crystal system	monoclinic	
Space group	*C*2/*c*	
Unit cell dimensions	a = 25.7389(3) Å	α = 90°
	b = 12.68950(10) Å	β = 96.8000(10)°
	c = 14.3223(2) Å	γ = 90°
Volume	4644.95(9) Å^3	
Z	8	
Density (calculated)	1.359 Mg/m^3	
Absorption coefficient	7.530 mm^{-1}	
F(000)	1944	
Crystal color, morphology	violet, needle	
Crystal size	0.149 x 0.05 x 0.038 mm^3	
Theta range for data collection	3.459 to 77.848°	
Index ranges	$-27 \leq h \leq 32$, $-15 \leq k \leq 15$, $-18 \leq l \leq 18$	
Reflections collected	20831	
Independent reflections	4840 [*R*(int) = 0.0333]	
Observed reflections	4615	
Completeness to theta = 74.504°	99.5%	
Absorption correction	Multi-scan	
Max. and min. transmission	1.00000 and 0.56703	
Refinement method	Full-matrix least-squares on F^2	
Data / restraints / parameters	4840 / 42 / 284	
Goodness-of-fit on F^2	1.061	
Final *R* indices [*I*>2sigma(*I*)]	*R*1 = 0.0340, *wR*2 = 0.0881	
R indices (all data)	*R*1 = 0.0355, *wR*2 = 0.0891	
Largest diff. peak and hole	0.516 and -0.615 e.Å^{-3}	

Chapter 3. The Synthesis, Characterization, and Electro- and Photochemical Investigation of an Iron Pyrazalonyl Complex

Introduction

Investigation into new earth-abundant first row transition metal catalysts is imperative to the quest to make hydrogen generation more economically and environmentally favorable. Previous studies by our group exhibit the process of designing and optimizing a family of highly effective electro- and photocatalysts for both homogeneous and heterogeneous catalytic systems. As shown in chapter 2, known effective catalysts can be modified with a variety of functional groups to alter some characteristics of the catalyst while maintaining structural and mechanical properties of the parent complex. It is therefore highly important to find new effective catalysts that can be modified and embedded into heterogeneous systems to further the library of catalysts for hydrogen generation.

A challenge with first row metal catalysts is the limitation of one electron processes. By incorporating a ligand that exhibits redox activity, multielectron reactions can occur more readily, as both the metal center and ligands can undergo redox processes simultaneously. Therefore, redox-active, or noninnocent, ligands are of great interest for catalysis, and they can allow for two electron reduction needed for HER that generally otherwise require heavier and more electron rich noble metals.[1-3] This makes noninnocent ligand complexes of great interest for hydrogen generation catalyst.

In 2011, McNamara et al. investigated a cobalt-diothiolene complex for its resistance to hydrogenation, reversible redox reactions, and ability to undergo multielectron chemistry for hydrogen generation, and found that the complex was able to generate over 2700 TONs in 1:1 H_2O:ACN $Ru(bpy)_3^{2+}$ and ascorbic acid system.[4]

In 2019, Li et al. introduced complexes with a redox-active salen ligand that was determined to be an active photocatalyst when complexed with nickel, generating over 350 TONs in 5.5 hours with an eosin Y chromophore.[5]

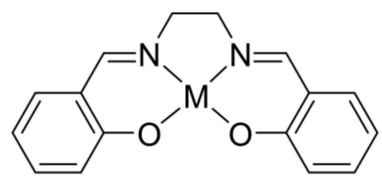

M= Ni(II), Cu(II), Zn(II)

Figure 3.1. Structure of metal-salen ligand complexes.[5]

Previous studies in our lab have also shown the benefit of utilizing redox-active ligands in first row transition metal catalysts. Wise et al. studied an active photocatalyst with a nickel and redox-active Bis-dithiocarbazate ligand complex that generated over 3300 TONs over 70 hours (Figure 3.2).[6]

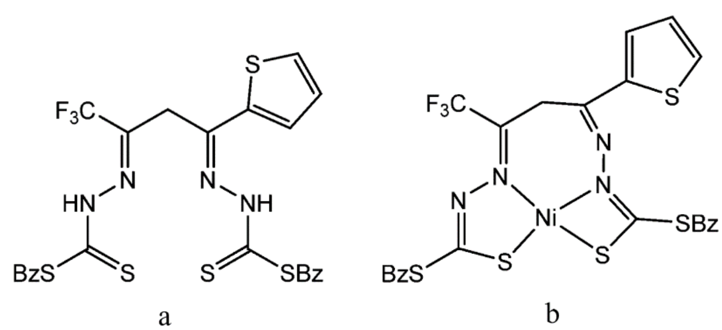

Figure 3.2. Redox-active Bis-dithiocarbazate ligand (**a**) and nickel catalyst (**b**).[6]

In this chapter, we introduce a N,N'- bis(4-antipyrlmethylidene) ethylenediamine (BAME) ligand (Figure 3.3). The ligand can be made in a facile one-pot synthesis method and is easily synthesized and complexed with first row transition metals. While this ligand has not been found to be used in previous research, it contains pyrazalone moieties that have been studied for medicinal applications.[7] It is a molecule of interest due to its Schiff base properties and ONNO coordination environments similar to salen ligands. BAME shows great promise for catalytic activity due to its redox-active nature and tetradentate-binding abilities. Herein, we describe the synthesis and coordination of BAME with iron (Figure 3.4), and the complex's structural characterization and assessment of electrochemical and photochemical abilities. The iron (III) N,N'-bis(4-antipyrlmethylidene)ethylenediamine (FeBAME) complex is also assessed for its ability to generate hydrogen in impure water systems in the hopes of creating a photocatalytic system that can generate both energy and clean water via hydrogen generation from natural water sources.

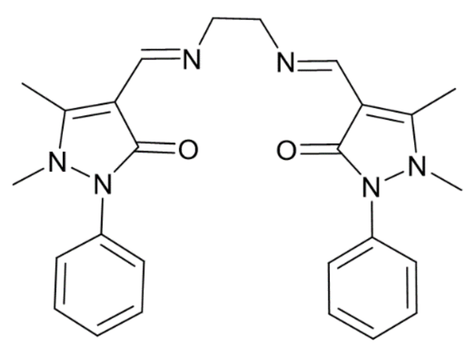

Figure 3.3. Structure of N,N'- bis(4-antipyrlmethylidene)ethylenediamine ligand.

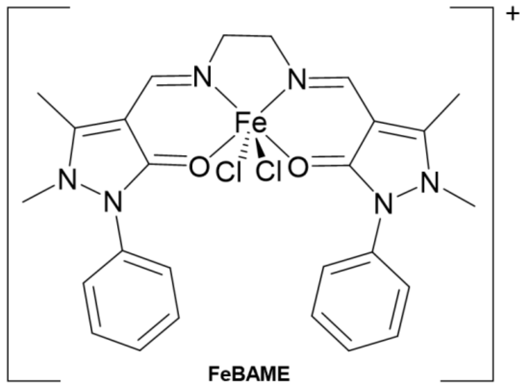

Figure 3.4. Structure of iron (III) N,N'- bis(4-antipyrlmethylidene) ethylenediamine complex.

Methods

Synthesis of N,N'-bis(4-antipyrylmethylidene)-ethylenediamine (BAME)

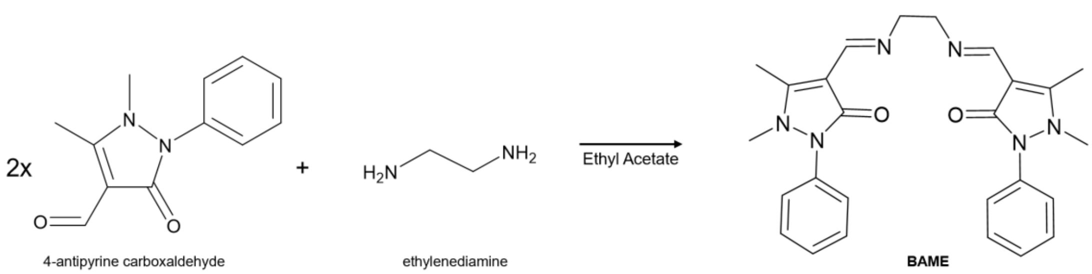

Figure 3.5. Synthesis procedure for BAME.

N,N'-bis(4-antipyrylmethylidene)ethylenediamine (BAME) was synthesized using a modified literature procedure (Figure 3.5).[8] In a 100 mL round-bottom flask containing 4-antipyrine carboxaldehyde dissolved in ethyl acetate, a solution of ethylenediamine in ethyl acetate was added dropwise. The solution was refluxed while stirring for 4 hours and the resulting crystalline solid was obtained by vacuum filtration and 3 rinses of ethyl acetate. The resulting solid was light yellow and confirmed using NMR (Figure B2).

Synthesis of **FeBAME**

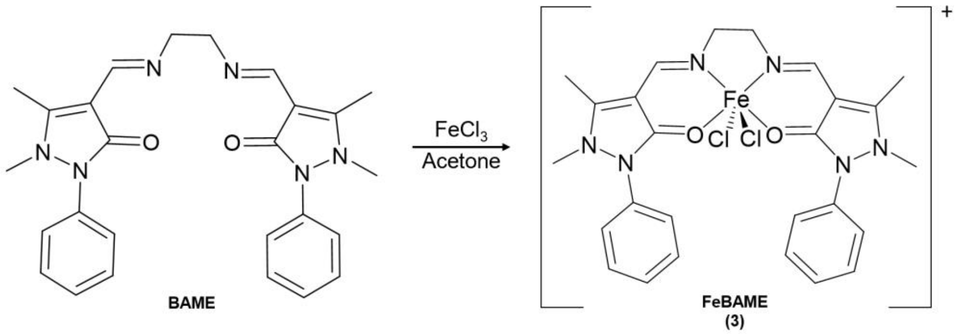

Figure 3.6. Complexation of $FeCl_3$ with BAME ligand.

Iron (III) N,N'- bis(4-antipyrlmethylidene)ethylenediamine was synthesized using a modified literature procedure (Figure 3.6).[9] In a 30 mL screw top vial, BAME was suspended in acetone. To this solution, $FeCl_3$•$6H_2O$ dissolved in acetone was added dropwise. Upon metal addition, the solution turned deep red, and the vessel was sealed and allowed to reflux while stirring for 1 hour. The solution was cooled and the precipitate collected using vacuum filtration, rinsed with acetone, and dried over vacuum. The complex was purified for electro- and photochemical studies using slow diffusion by layering a highly concentrated solution of **3** in methanol with ethyl acetate. Red needle crystals formed over 24 hours, the mother liquor was decanted, and the crystals were dried and collected. Crystals for structural characterization were made with a slow diffusion of ethyl ether into a highly concentrated solution of **3.** The complex was characterized using x-ray crystallography and high resolution mass spectrometry. High resolution mass spectrometry for $C_{26}H_{28}Cl_2FeN_6O_2^+$: predicted m/z=582.099473, observed m/z=582.099886 (Figure B3).

Electrochemical Measurements:

Cyclic Voltammetry

All electrochemical experiments were performed under an argon atmosphere using CH Instruments 620D potentiostat and CH Instruments 680 amp booster. Cyclic voltammograms (CV) were taken using a standard three-electrode cell, including a saturated calomel electrode (SCE), platinum auxiliary electrode, and glassy carbon working electrode. The platinum and glassy carbon electrodes were polished prior to each CV using 0.05 μm alumina powder on a cloth-covered polishing pad and rinsed thoroughly with deionized water and acetonitrile.

Scan Rate Dependence Study

5.0 mL acetonitrile, 0.2 g tetrabutylammonium hexafluorophosphate ($TBAPF_6$, 0.1M), and 0.3 mg of FeBAME (0.1 mM) were added to an electrochemical cell and degassed with argon for 12 minutes. CVs were taken at a potential range from -0.1 to -1.6 V vs Fc^+/Fc with scan rates ranging from 50-900 mV/s.

Acid Addition Study

5.0 mL acetonitrile, 0.2 g tetrabutylammonium hexafluorophosphate ($TBAPF_6$, 0.1M), and 0.3 mg of **3** (0.1 mM) were added to an electrochemical cell and degassed with argon for 12 minutes. CVs were taken without acid, and after the addition of 10, 20, 30, 40, and 50 uL of 0.11 M trifluoroacetic acid (TFA). The CV was taken at a potential range from -0.1 to -1.6 V vs Fc^+/Fc with a scan rate of 0.2 V/s.

Photochemical Measurements:

Hydrogen Evolution Studies

Hydrogen evolution was determined using test tubes with 1:1 ethanol: deionized water solvent, varying amounts of FeBAME, 1.8 mM fluorescein, and 5% triethylamine (TEA, v/v%). Immediately after the addition of TEA, test tubes were sealed with a septa and copper wire and degassed with argon for 10 minutes. A Hamilton syringe was used to remove 1.0 mL argon from the headspace of the test tube and then 1.0 mL of methane was added as an internal standard. The test tubes were irradiated with green light (560 nm wavelength) while stirring. After irradiation, 0.10 mL of headspace was removed using a Hamilton gas syringe and injected into a gas chromatograph to determine the ratio of hydrogen to methane to determine hydrogen produced.

System Optimization Studies

The general procedure for hydrogen evolution studies was followed while varying catalyst or chromophore concentration. Comparison of TONs were made between 5, 10, 30, 60, and 180 μL of **3** and 1.0, 1.4, and 1.8 mM fluorescein in EtOH solutions. Studies of best chromophore and SED pairing were also done by comparing the TONs between fluorescein with TEA, eosin Y with TEA, eosin Y and TEOA, or eosin Y and TEOA at pH 7.

Results and Discussion

Crystals of **3** were obtained via slow diffusion into diethyl ether from a highly concentrated solution of **3** in methanol. X-ray crystallography was performed on a red crystal with plate morphology, and it was determined **3** had an orthorhombic lattice structure. The iron center had a distorted octahedral structure, with all Fe-N and Fe-O bonds between 2.02 and 2.13 Å, and the Fe-Cl bonds were slightly longer at 2.33-2.36 Å. Octahedral complexes typically have axial positions 180° apart and equatorial positions 90° apart. The main distortions in the octahedral complex occur in the O(1)-Fe-O(2) 103° bond angle and N(2)-Fe-N(1) 76.8° bond angle, with all other bond angles within 10% difference from the 180° and 90° expected angles (Figure 3.7, Table 3.1). The length of the O(1)-C(5) and O(2)-C(17) bonds are 1.27-1.28 Å, which is consistent with the length of a CO double bond.

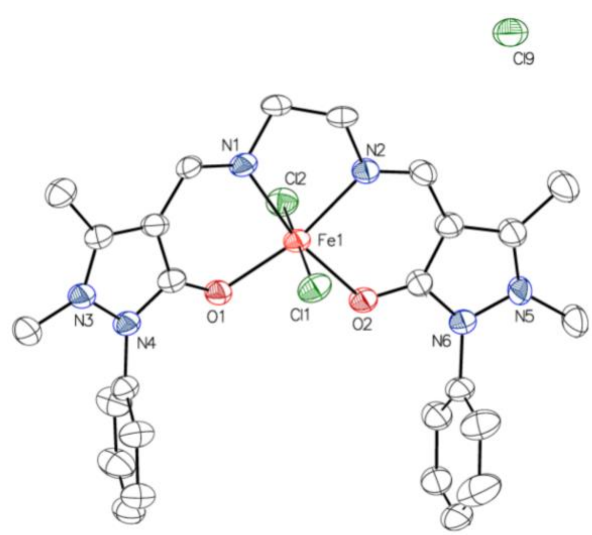

Figure 3.7. ORTEP diagram of **3**. Fe (orange), O (red), Cl (green), N (blue), C (white). Ellipsoids are at the 50% probability level and all hydrogen atoms have been omitted for visual clarity.

Table 3.1. Bond lengths and angles of Fe for **3**

Bond	Bond Lengths (Å)
Fe(1)-Cl(1)	2.3606(15)
Fe(1)-Cl(2)	2.3339(15
Fe(1)-O(1)	2.016(3)
Fe(1)-N(2)	2.030(3)
Fe(1)-N(1)	2.131(4)
Fe(1)-N(2)	2.126(4)
O(1)-C(5)	1.286(6)
O(2)-C(17)	1.269(6)
Bonds	**Bond angles (°)**
Cl(1)-Fe(1)-Cl(2)	175.04(5)
O(1)-Fe(1)-Cl(1)	86.56(11)
O(1)-Fe(1)-Cl(2)	92.15(11)
O(1)-Fe(1)-O(2)	102.95(13
O(1)-Fe(1)-N(1)	89.16(14)
O(1)-Fe(1)-N(2)	165.54(14)
O(1)-Fe(1)-Cl(1)	86.28(11)
O(2)-Fe(1)-Cl(2)	89.34(11)
O(2)-Fe(1)-N(1)	167.88(15)
O(2)-Fe(1)-N(2)	91.11(15)
N(1)-Fe(1)-Cl(1)	94.66(12)
N(1)-Fe(1)-Cl(2)	90.11(12)
N(2)-Fe(1)-Cl(1)	91.08(13)
N(2)-Fe(1)-Cl(2)	91.35(13)
N(2)-Fe(1)-N(1)	76.80(16)

The UV/Vis spectrum of **3** indicates absorptions at 360 and 490 nm. The absorption at 360 nm is indicative of a π-π^* transition within the ligand and the absorption at 490 nm is indicative of ligand to metal charge transfer (LMCT, Figure 3.8).[10]

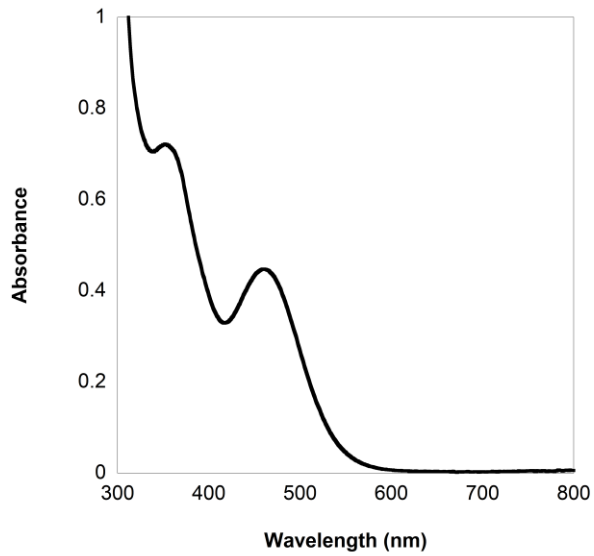

Figure 3.8. UV/vis spectrum of **3** in DCM.

Electrochemical analysis was performed on **3** to determine the electrocatalytic abilities. To assess **3** for the ability to reduce protons, CVs from -0.1 to -1.6 V vs. Fc^+/Fc were taken without acid and with increasing aliquots of 0.11 M TFA. A reversible reduction event corresponding to Fe(III) to Fe(II) occurs at -0.43 V vs Fc^+/Fc and does not shift with the addition of a proton source. This indicates that the reaction mechanism is ECCE or ECEC, where the primary step of catalysis is a reduction event (E), followed by a protonation chemical event (C). Upon addition of a proton source, an irreversible catalytic wave occurs at -1.47 V vs Fc^+/Fc and increases with each 10 uL 0.11M TFA addition (Figure 3.8).

Further electrochemical investigations must be done to reveal the rate-dependance on the proton and catalyst concentrations.

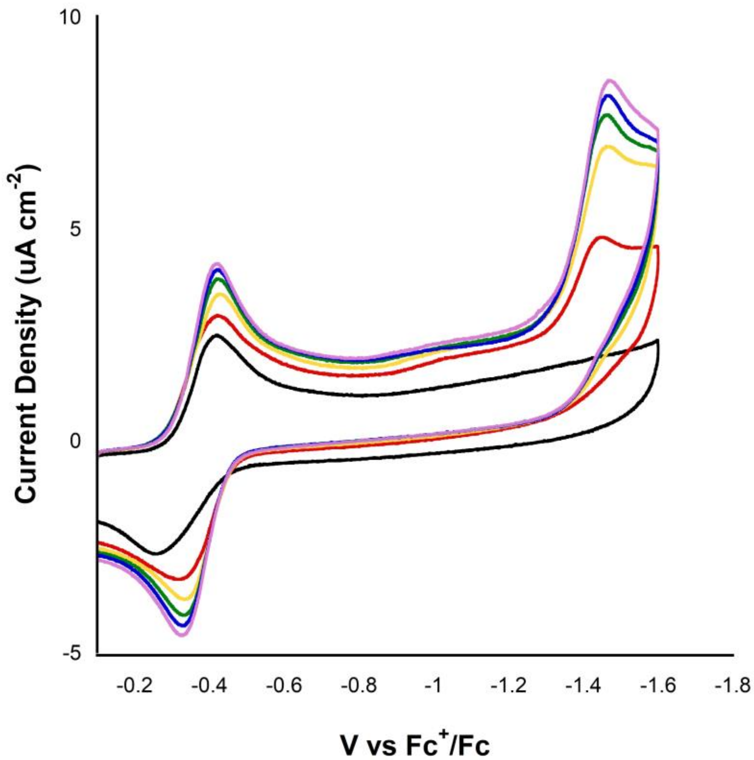

Figure 3.9. CV of **3** with no acid (black), and 0.22 (red), 0.44 (yellow), 0.66 (green), 0.88 (blue) and 1.1 mM (purple) TFA.

3 was found to be catalytically active for proton reduction, as determined by its i_c / i_p of 5.27 with the addition of 1.1 mM TFA proton source. **3** was found to operate at an overpotential of 690 mV in 1.1 mM TFA in ACN. The overpotential was calculated by subtracting the literature value for proton reduction in 1 mM TFA from the half-wave potential of the irreversible catalytic wave of proton reduction.[11]

$$\text{Overpotential}=|E_{1/2\ \text{wave}} - E_{\text{ref}}|$$

$$=|(-1.4\ \text{V}) - (-0.71\ \text{V})|$$

$$=0.69\ \text{V} = 690\ \text{mV}$$

After **3** was analyzed for its electrocatalytic abilities, it was then incorporated into a photocatalytic system to assess its ability to generate hydrogen using light. Two organic chromophores, fluorescein and eosin Y, were assessed with TEA or TEOA sacrificial electron donors. Fluorescein and TEA were found to be the best candidates, and Fl concentrations were found to be optimized at 1.8 mM. Catalyst concentration studies found the greatest TONs with 10 nM concentration of **3.**

Time course studies of **3** illustrated that the photocatalyst generated hydrogen for over 60 hours with a maximum TON of 2,379 (Figure 3.9). This illustrates the longevity of **3** and implies its stability in aqueous solutions during irradiation.

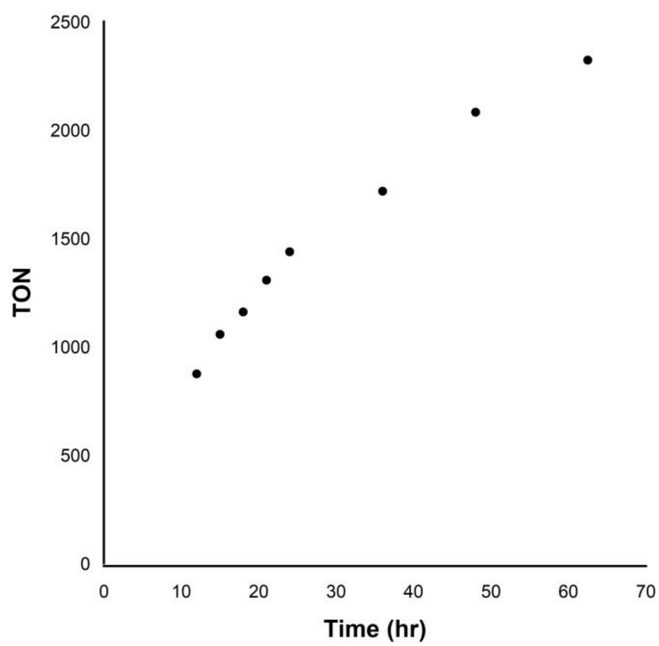

Figure 3.10. TONs over 62 hours in 2.1 mM Fl, 5% TEA, and 10 nM **3** 1:1 H_2O:EtOH photochemical system.

Natural Water Studies:

One ultimate goal of photocatalysts for hydrogen generation is to make energy more accessible to everyone. In order for this to be possible, the catalyst must be robust enough to be used in impure water systems, as access to deionized water is very limited. With this goal in mind, various water sources were assessed for the ability to generate hydrogen in a photocatalytic system. Water was collected from Lake Matoaka in Williamsburg, Buckroe Beach in Hampton, VA, and Virginia Beach, VA. The water was collected in a glass jar, sealed, and stored in a refrigerator until use. The water was then brought to room temperature and filtered through a celite filter under vacuum filtration to remove sand or precipitate, and then used in place of DI water in the photocatalytic system. When TEA was added to the water samples before adding to the photochemical cells, large amounts of white precipitate formed. Due to this precipitate, catalyst concentrations had to be increased to generate hydrogen. This explicates the need for optimization in each set of photochemical conditions.

The lake, bay, and sea water trials were found to generate hydrogen for over 30 hours, with maximum TONs reaching 803 for lake water, 269 for bay water, and 330 for seawater (Figure 3.10). Lake water was found to produce TONs of roughly half of TONs found in the optimized DI water system, which is consistent with TON percent decrease found in previous studies by Hartley et al.[12]

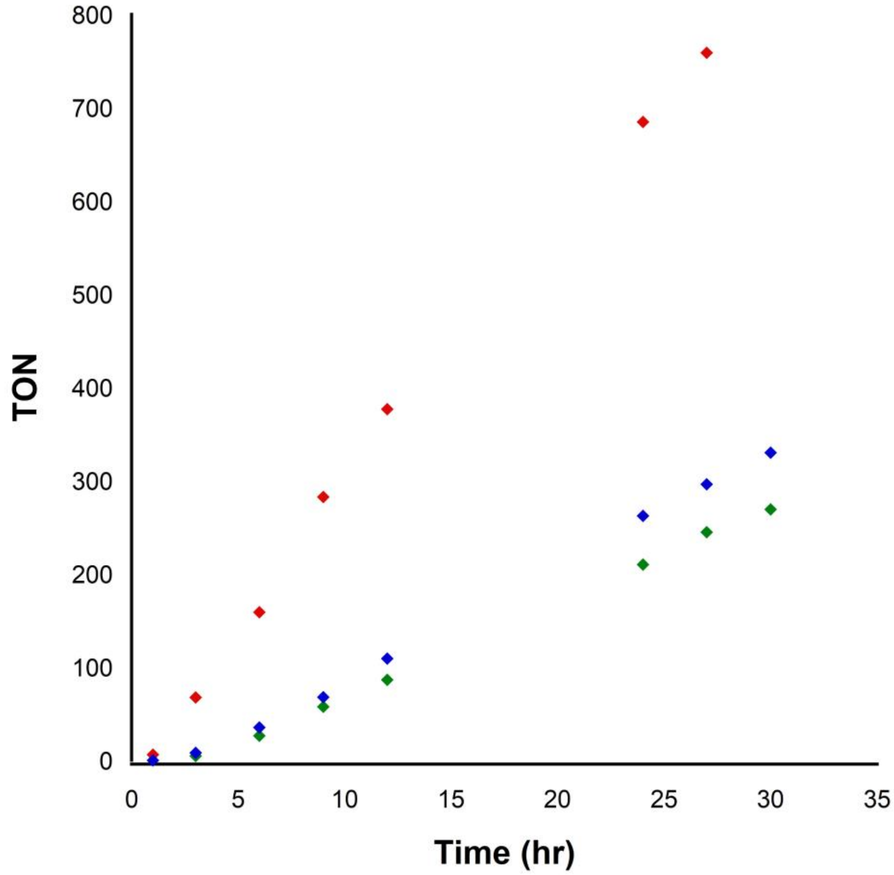

Figure 3.11. TONs over 30 hours for lake (red) , bay (green), and sea (blue) waters.

Conclusion

In conclusion, a novel iron catalyst has been synthesized, characterized, and shown to be effective in electrochemical and photochemical proton reduction. **3** was shown to be more efficient than previously studied iron catalyst with an overpotential of 690 mV and is electrocatalytically active, with an i_c/i_p of 5.27. **3** was also shown to be an effective photocatalyst in a system consisting of a fluorescein chromophore and TEA sacrificial electron donor, and exhibited over 2,300 TON over 60 hours. Testing in natural water sources proved **3** to be a robust photocatalyst that is able to generate hydrogen in impure systems, implying that the catalyst has potential to be used in non-laboratory settings for clean energy generation and water purification in many parts of the world and beyond. **3** has shown great potential for HER catalysis and may be a good candidate for further research and modification studies. Future research may include complexing BAME with other transition metals. Complexing with non-redox-active metals, such as zinc, can allow for electrochemical assessment of the noninnocence of the BAME ligand. Future complexes may also be assessed for catalytic ability in the hydrogen evolution reaction, oxygen reduction reaction, and CO_2 reduction reaction.

References

1. Eisenberg, R.; Gray, H. B. Noninnocence in Metal Complexes: A Dithiolene Dawn. *Inorg. Chem.* **2011**, *50* (20), 9741–9751. https://doi.org/10.1021/ic2011748.
2. Kaim, W. Manifestations of Noninnocent Ligand Behavior. *Inorg. Chem.* **2011**, *50* (20), 9752–9765. https://doi.org/10.1021/ic2003832.
3. Luca, O. R.; Crabtree, R. H. Redox-Active Ligands in Catalysis. *Chem. Soc. Rev.* **2013**, *42* (4), 1440–1459. https://doi.org/10.1039/C2CS35228A.
4. McNamara, W. R.; Han, Z.; Yin, C.-J. (Madeline); Brennessel, W. W.; Holland, P. L.; Eisenberg, R. Cobalt-Dithiolene Complexes for the Photocatalytic and Electrocatalytic Reduction of Protons in Aqueous Solutions. Proc. Natl. Acad. Sci. 2012, 109 (39), 15594–15599. https://doi.org/10.1073/pnas.1120757109.
5. Li, C.-B.; Chu, Y.; He, J.; Xie, J.; Liu, J.; Wang, N.; Tang, J. Photocatalytic Hydrogen Production Based on a Serial Metal-Salen Complexes and the Reaction Mechanism. *ChemCatChem* **2019**, *11* (24), 6324–6331. https://doi.org/10.1002/cctc.201901656.
6. Wise, C. F.; Liu, D.; Mayer, K. J.; Crossland, P. M.; Hartley, C. L.; McNamara, W. R. A Nickel Complex of a Conjugated Bis-Dithiocarbazate Schiff Base for the Photocatalytic Production of Hydrogen. *Dalton Trans.* **2015**, *44* (32), 14265–14271. https://doi.org/10.1039/C5DT02042E.
7. *Antipyrine-Benzocaine Otic: MedlinePlus Drug Information*. https://medlineplus.gov/druginfo/meds/a607073.html (accessed 2023-04-06).
8. Joseph, S.; Radhakrishnan, P. K. Yttrium and Lanthanide Iodide Complexes of N,N′-Bis(4-Antipyrylmethylidene)Ethylenediamine. *Polyhedron* **1999**, *18* (13), 1881–1884. https://doi.org/10.1016/S0277-5387(98)00432-X.
9. *Complexes of Iron(III) with N,N′-bis(4-Antipyrylmethylidene)ethylenediamine: Synthesis and Reactivity in Inorganic and Metal-Organic Chemistry: Vol 33, No 1*. https://www.tandfonline.com/doi/abs/10.1081/SIM-120016870?journalCode=lsrt19 (accessed 2023-04-06).
10. Lanznaster, M.; Neves, A.; Bortoluzzi, A. J.; Assumpção, A. M. C.; Vencato, I.; Machado, S. P.; Drechsel, S. M. Electronic Effects of Electron-Donating and -Withdrawing Groups in Model Complexes for Iron-Tyrosine-Containing Metalloenzymes. Inorg. Chem. 2006, 45 (3), 1005–1011. https://doi.org/10.1021/ic050869o.
11. Fourmond, V.; Jacques, P.-A.; Fontecave, M.; Artero, V. H2 Evolution and Molecular Electrocatalysts: Determination of Overpotentials and Effect of Homoconjugation. *Inorg. Chem.* **2010**, *49* (22), 10338–10347. https://doi.org/10.1021/ic101187v.
12. Hartley, C. L.; DiRisio, R. J.; Screen, M. E.; Mayer, K. J.; McNamara, W. R. Iron Polypyridyl Complexes for Photocatalytic Hydrogen Generation. *Inorg. Chem.* **2016**, *55* (17), 8865–8870. https://doi.org/10.1021/acs.inorgchem.6b01413.

Appendix B

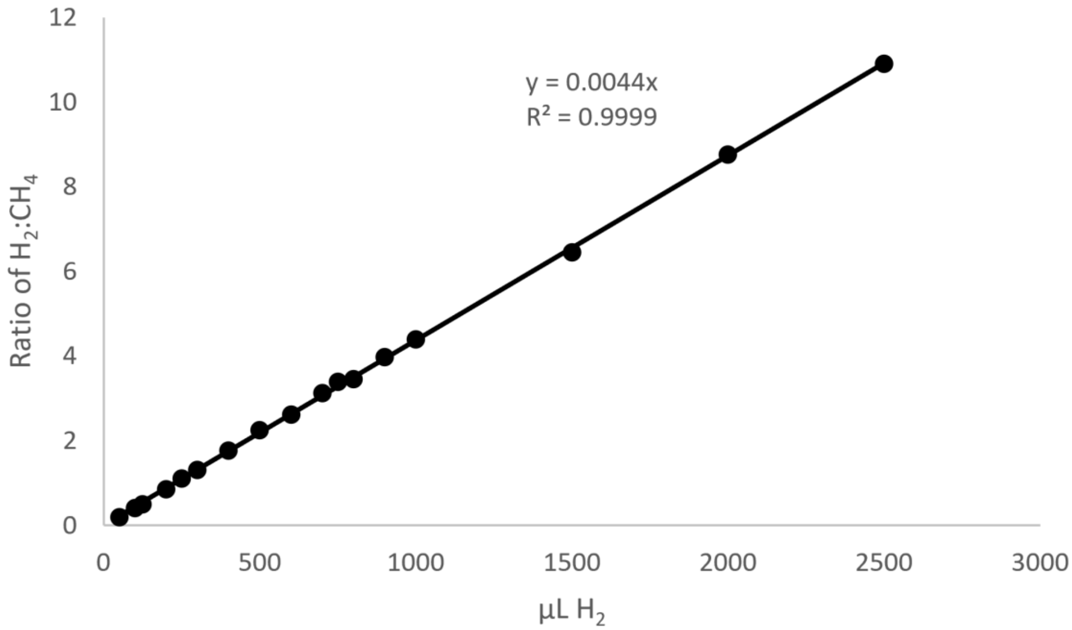

Figure B1. Calibration curve relating µL hydrogen generated to the ratio of the area of H_2 to CH_4 peaks in GC

Turnover number (TON) is defined as the moles of product generated per mole of catalyst. To determine the TON for hydrogen generated by our catalyst, a calibration curve has been developed by injecting a known amount of hydrogen, as well as the internal standard, methane, into the gas chromatograph (GC). The ratio of the obtained hydrogen and methane peaks are then plotted versus the volume of injected hydrogen. The calibration curve used for this study resulted in a slope of 0.0044 and is used to determine the volume, and therefore moles, of hydrogen generated from the system.[7] The equation is as follows:

$$\mu L\ H_2 = \frac{1}{0.0044}\left(\frac{Area\ H_2}{Area\ CH_4}\right)$$

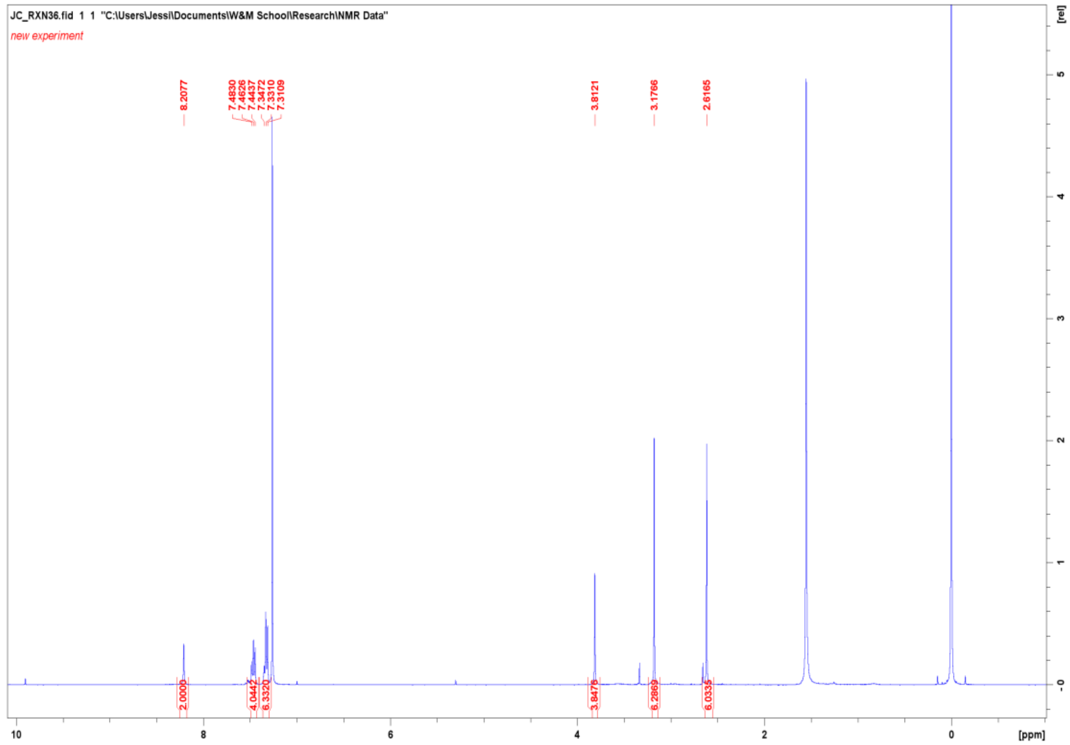

Figure B2. ^{1}H NMR of BAME ligand with integrations and shifts.

Sample Name	FeBAME in MeOH			
Exact Mass of	$C_{26}H_{28}Cl_2FeN_6O_2$ +	=	582.099473	m/z
Mass Observed		=	582.099886	m/z

Difference < 1.0 ppm

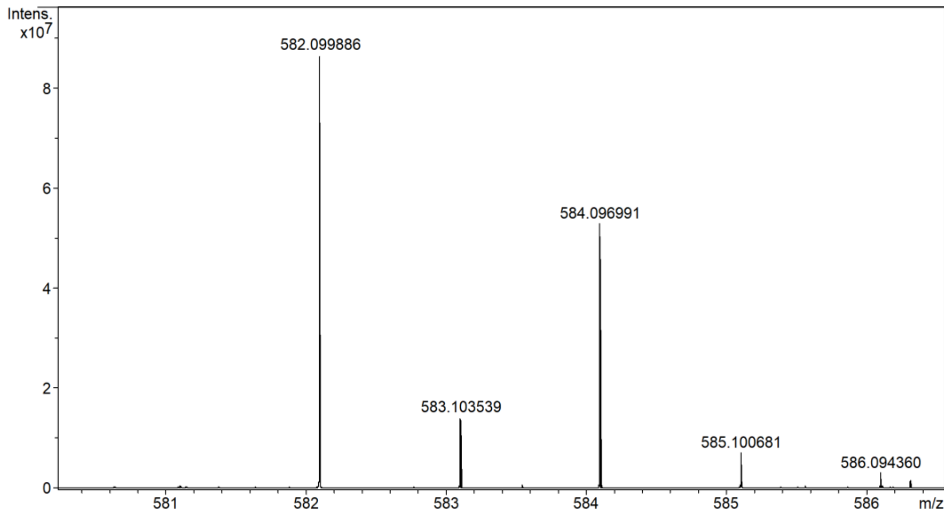

Figure B3. High resolution mass spectrometry results of **3**. The expected molecular ions were observed with a difference of less than 1 ppm.

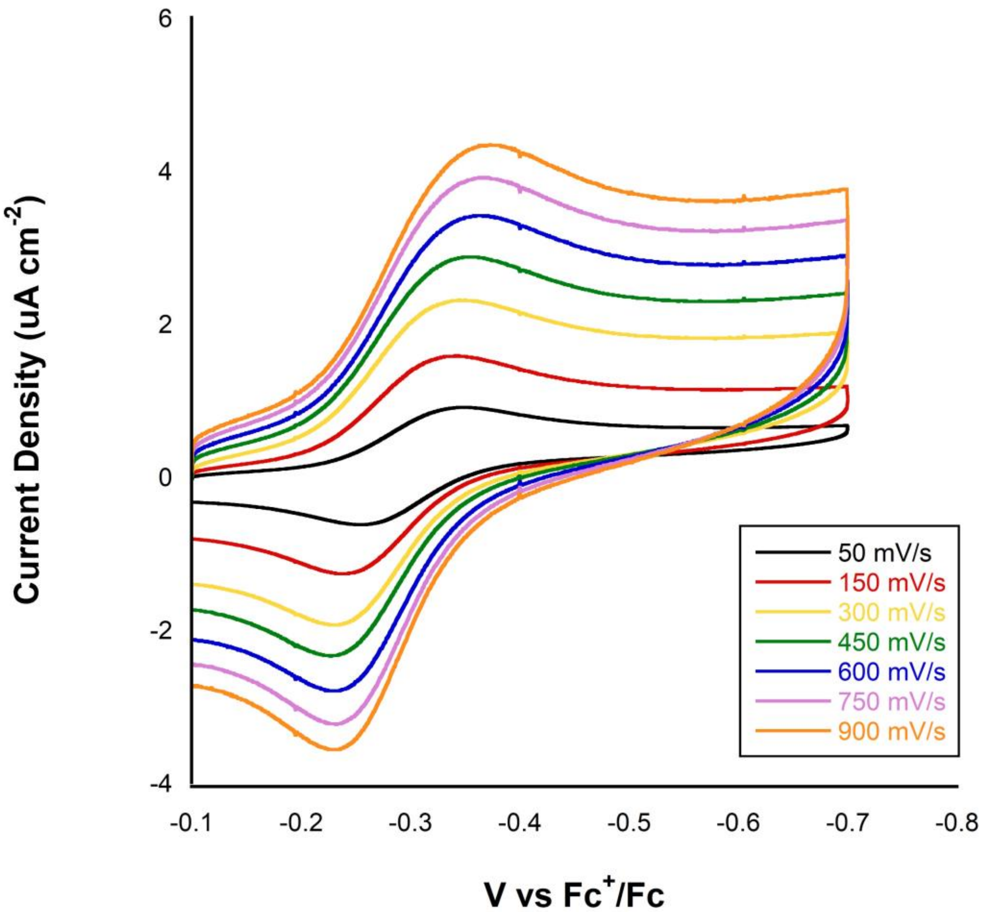

Figure B4. Scan rate study of **3** with scan rates varying from 50-900 mV/s.

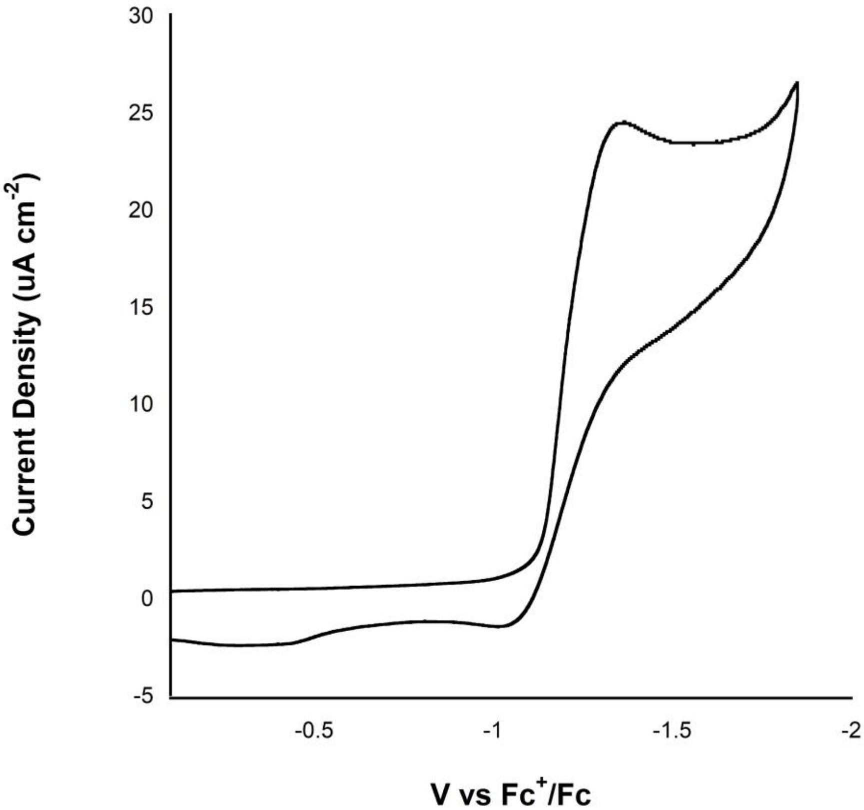

FIgure B5. CV of **BAME** ligand in 0.1 M $TBAPF_6$ and ACN

Table. B1

Chromophore/ electron donor	Fl/TEA	EY/TEA	EY/TEOA	EY/TEOA pH 7
TON with 60 nM **3**	208	51	46	0

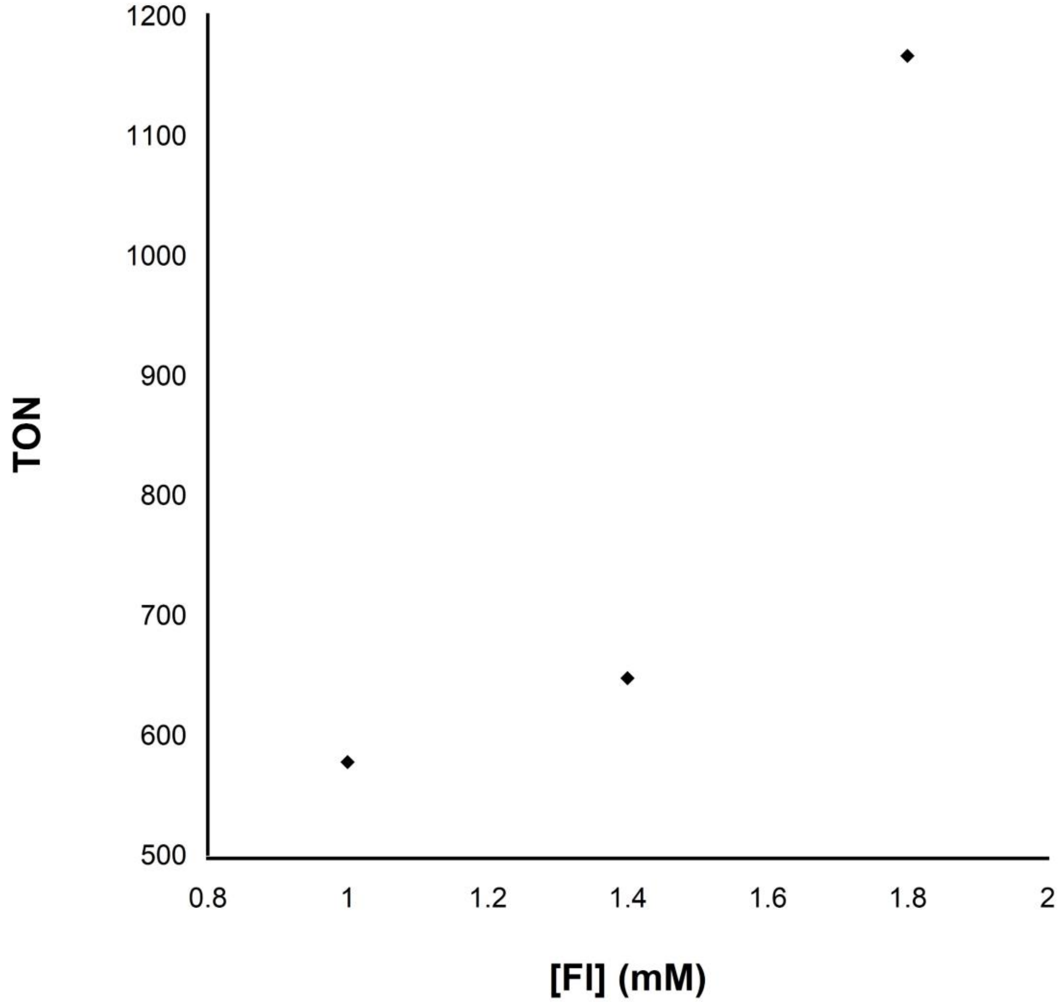

Figure B6. TON vs. [Fl] (mM) with 30 nM **3** and 5% TEA in 1:1 H_2O:EtOH after 24 hours.

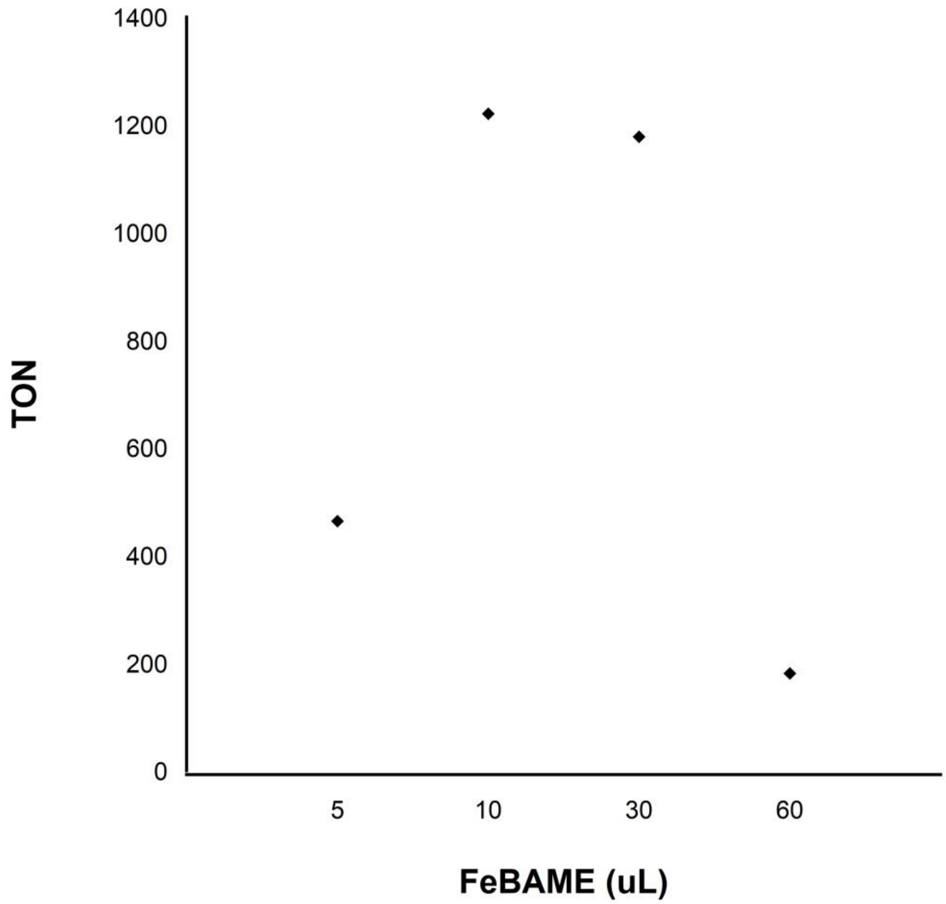

Figure B7. TON vs. [**3**] (μL) with 1.8 mM Fl and 5% TEA in 1:1 H_2O:EtOH after 24 hours.

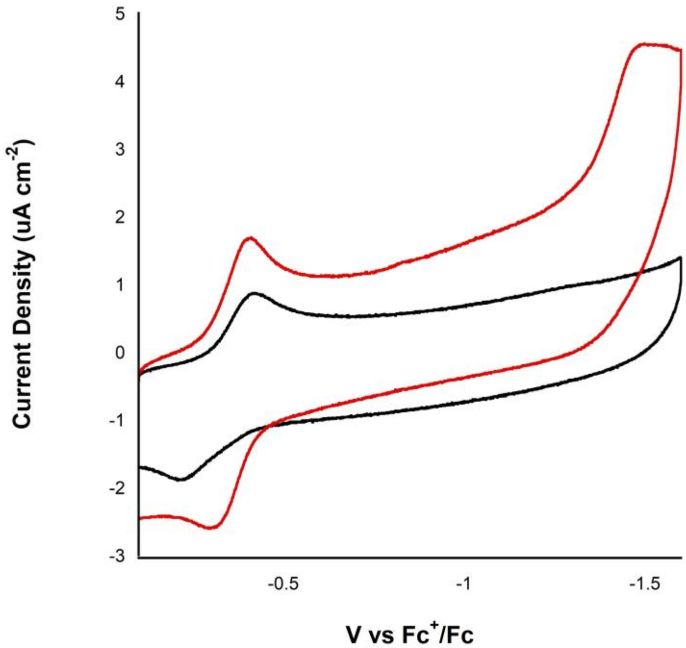

Figure B8. CV of **3** before (black) and after (red) the addition of 1.1mM TFA used to determine i_c /i_p of 5.27

Table B2. Crystal data for **3**

Identification code	cwmwm18	
Empirical formula	C26 H28 Cl3 Fe N6 O2	
Formula weight	618.74	
Temperature	100.00(10) K	
Wavelength	1.54184 Å	
Crystal system	orthorhombic	
Space group	$P2_12_12_1$	
Unit cell dimensions	a = 18.0494(2) Å	α = 90°
	b = 26.5169(2) Å	β = 90°
	c = 28.1081(2) Å	γ = 90°
Volume	13452.9(2) $Å^3$	
Z	16	
Density (calculated)	1.222 Mg/m^3	
Absorption coefficient	6.032 mm^{-1}	
F(000)	5104	
Crystal color, morphology	red, plate	
Crystal size	0.241 x 0.209 x 0.081 mm^3	
Theta range for data collection	3.353 to 81.549°	
Index ranges	$-23 \leq h \leq 22$, $-26 \leq k \leq 33$, $-35 \leq l \leq 35$	
Reflections collected	136133	
Independent reflections	28760 [R(int) = 0.0465]	
Observed reflections	25201	
Completeness to theta = 67.684°	100.0%	
Absorption correction	Multi-scan	
Max. and min. transmission	1.00000 and 0.51928	
Refinement method	Full-matrix least-squares on F^2	
Data / restraints / parameters	28760 / 99 / 1452	
Goodness-of-fit on F^2	1.044	
Final R indices [I>2sigma(I)]	$R1$ = 0.0493, $wR2$ = 0.1240	
R indices (all data)	$R1$ = 0.0577, $wR2$ = 0.1295	
Absolute structure parameter	0.052(4)	
Largest diff. peak and hole	0.745 and -0.614 e.$Å^{-3}$	